SEDIMENTOLOGY
the journal of the
International Association of Sedimentologists

Formation of Mg-silicates in the microbial sediments of a saline, mildly alkaline coastal lake (Lake Clifton, Australia): environmental versus microbiological drivers

Journal:	*Sedimentology*
Manuscript ID	SED-2024-OA-090.R3
Manuscript Type:	Original Article
Date Submitted by the Author:	n/a
Complete List of Authors:	Mercedes-Martín, Ramon; Universitat Autonoma de Barcelona, Geology Sánchez-Román, Mónica; Vrije Universiteit Amsterdam, Department of Earth Sciences Ayora, Carlos; Departament de Geociències, Institut de Diagnosi Ambiental i Estudis de l'Aigua (IDÆA-CSIC) Rogerson, Mike; Northumbria University, Geography and Environmental Science Thomas, Camille; Institute of Geological Sciences & Oeschger Centre for Climate Research, University of Bern, Baltzerstrasse 1+3 Van Spanning, Rob; Section Molecular Microbiology, A-LIFE, AIMMS, Vrije Universiteit Amsterdam, Amsterdam, The Netherlands Brasier, Alexander; University of Aberdeen, School of Geosciences Wacey, David; Centre for Microscopy Characterisation and Analysis, The University of Western Australia, Perth, WA 6009, Australia Reijmer, John; Vrije Universiteit Amsterdam, Earth Sciences Department, Faculty of Science, De Boelelaan 1086, 1081 HV Amsterdam, The Netherlands
Keywords:	Mg-silicate, lacustrine, diagenesis, diatom, microbial, geochemistry

Formation of Mg-silicates in the microbial sediments of a saline, mildly alkaline coastal lake (Lake Clifton, Australia): environmental versus microbiological drivers

Ramon Mercedes-Martín[1]*, Mónica Sánchez-Román[2], Carlos Ayora[3], Mike Rogerson[4], Camille Thomas[5], Rob Van Spanning[6], Alex Brasier[7], David Wacey[8], and John J. Reijmer[2]

1. Universitat Autònoma de Barcelona, Department of Geology, Edifici Cs, 08193, Cerdanyola del Vallés, Spain. *ramon.mercedes@uab.cat
2. Vrije Universiteit Amsterdam, Earth Sciences Department, Faculty of Science, De Boelelaan 1086, 1081 HV Amsterdam, The Netherlands.
3. Departament de Geociències, Institut de Diagnosi Ambiental i Estudis de l'Aigua (IDÆA-CSIC), Barcelona, Spain.
4. Department of Geography and Environmental Science, Ellison Building, Northumbria University, Newcastle, UK, NE1 8ST.
5. Institute of Geological Sciences & Oeschger Centre for Climate Change Research, University of Bern, Baltzerstrasse 1+3, 3012 Bern, Switzerland.
6. Section Molecular Microbiology, A-LIFE, AIMMS, Vrije Universiteit Amsterdam, Amsterdam, The Netherlands.
7. School of Geosciences, Meston Building, University of Aberdeen, Old Aberdeen, Scotland, UK, AB24 3UE.
8. Centre for Microscopy Characterisation and Analysis, The University of Western Australia, Perth, WA 6009, Australia

ABSTRACT

Recent interest in Mg-rich silicate formation stems from their role as valuable paleoclimatic indicators in fluvio-lacustrine environments and their insights into metal geochemical cycling. Traditionally, Mg-silicate genesis in lacustrine contexts is linked to alkaline or saline conditions in closed, evaporitic basins. However, the discovery of interparticle amorphous kerolite-like Mg-silicates in the sediments of Lake Clifton, a currently hypersaline coastal lagoon in Western Australia with circumneutral pH and moderate alkalinity, challenges existing models.

In this study, petrographic, hydrochemical, and microbial genomic data from different Lake Clifton sub-environments (episodically submerged and subaerial settings) and substrates (pustular microbial mats and non-lithifying microbial sediments) were integrated with geochemical modelling to quantify the mechanisms underlying the formation of Mg-silicates and aragonite peloids as lake shoreline sediments.

Geochemical modelling suggests that neither evaporation-driven alkalinity fluctuations nor mixing of lake water with groundwater can solely explain the kerolite-like/carbonate association observed in lakebed sediments. Kerolite-like phases nucleate in association with twisted microbial extracellular polymeric substances (EPS) and organic-rich bacterial remains; this, combined with the identification of diatom- and cyanobacteria-powered photosynthesis, putative anoxygenic photosynthesis, and sulphate-reducing metabolisms, suggests an intimate link between biologically induced processes and the co-precipitation of aragonite peloids and interparticle kerolite-like phases in the lake. Moreover, the contribution of dead diatom frustule dissolution towards kerolite-like authigenesis was geochemically simulated, revealing that the precipitation of observable amounts of kerolite-like at pH values measured in Lake Clifton waters would prevent the formation of aragonite, questioning the feasibility of a scenario dominated by large inputs of dissolved biogenic silica.

Discovery of kerolite-like Mg-silicates in microbial-bearing sediments of a hypersaline coastal lagoon prompts a holistic re-evaluation of the environmental and microbiological factors influencing Mg-silicate-carbonate co-precipitation in lacustrine-peri-marine settings.

Studying modern Mg-silicate-bearing lacustrine sediments offer the opportunity to better

understand the early diagenetic biotic- abiotic processes that may have had limited petrographic preservation potential in ancient saline lake deposits.

1. INTRODUCTION

The formation of Mg-rich silicates has garnered substantial interest in recent decades because these minerals can be employed as paleoclimatic recorders in fluvio-lacustrine environments (Millot, 1970; Jones, 1986; Calvo *et al.*, 1999; Galan & Singer, 2011; Deocampo & Jones, 2014), offer crucial information on the geochemical cycling of Si, Mg, K, or Ca in sedimentary basins (Badaut & Risacher, 1983; Tosca *et al.*, 2011; Milesi *et al.*, 2020; Muller *et al.*, 2023), and play substantial roles in templating early diagenetic mineral phases (Gac *et al.*, 1977; Darragi & Tardy, 1987; Souza-Egipsy *et al.*, 2005; Burne *et al.*, 2014; Kremer *et al.*, 2019; Molnár *et al.*, 2021). Mg-silicate minerals (e.g., stevensite, sepiolite, kerolite, or talc) form volumetrically significant deposits in lacustrine settings commonly associated with alkaline and/or saline conditions developed in hydrologically closed and evaporitic basins (Millot, 1970; Calvo *et al.*, 1999; Deocampo & Jones, 2014). These environments tend to feature a range of pH, alkalinities, salinities, pCO_2, Mg/Si ratios, and cation chemistries favouring the formation of many Al-free, Mg-silicate minerals such as sepiolite ($Mg_4(Si_6O_{15})(OH)_2{\cdot}6H_2O$), kerolite [$Mg_3Si_4O_{10}(OH)_2 \cdot nH_2O$ (n~1)], stevensite [$(Ca,Na)_xMg_{3-x}(Si_4O_{10})(OH)_2$], or talc [$Mg_3Si_4O_{10}(OH)_2$] (Jones, 1986; Jones & Galan, 1988; Deocampo, 2005; Velde & Meunier, 2008; Bristow & Milliken, 2011; Tosca & Masterson, 2014; Tosca, 2015; Baldermann *et al.*, 2018). Previous laboratory work has helped elucidate the chemical and biological constraints involved in Al-free, Mg-rich silicate neoformation (Bontognali *et al.*, 2014; Tosca & Masterson, 2014; Tosca, 2015; Baldermann *et al.*, 2018; Arizaleta *et al.*, 2020; Buey *et al.*, 2023); however, understanding and predicting how physico-chemical and biological drivers work in tandem to form these minerals in natural environments remains a challenge. Difficulties arise from determining whether nucleation and growth of these solid precipitates takes place homogeneously from solution (generally described as neoformation), or on the surface of a pre-existing material (commonly referred to as heterogeneous or epitaxial growth, Meldrum & Cölfen, 2008; Tosca, 2015; Pozo & Calvo, 2018), placing distinctive thermodynamic and kinetics barriers on their formation.

In the lacustrine sedimentary record, discrimination between Mg-silicate deposits formed by homogeneous or heterogeneous crystallisation is often not straightforward (Bristow & Milliken, 2011, and references therein), being particularly complex because Al-free, Mg-rich silicate minerals are prone to dissolution and early diagenetic transformations (Tosca & Wright, 2018; Mulders & Oelkers, 2020). Therefore, the integration of field, laboratory, and numerical approaches is critical to shed light on the multiple mechanisms contributing to the nucleation, growth, and preservation of Mg-silicate sediments in lacustrine environments (Tutolo & Tosca, 2018; Mercedes-Martín *et al.*, 2019; Arizaleta *et al.*, 2020; Milesi *et al.*, 2020). Central to this understanding is the recognition that the early nucleation of a more soluble and hydrated precursor phase with short range order (often amorphous) generally precedes the formation of a crystalline Mg-silicate mineral (Gac *et al.*, 1977; Calvo *et al.*, 1999; Buey *et al.*, 2000; Tosca, 2015; Besselink *et al.*, 2020). Amorphous precursor phases have been routinely identified in ancient continental clay successions (Buey *et al.*, 2000), however, the majority of these poorly crystalline phases have been documented in modern alkaline, saline lakes and/or coastal lagoons in close association with bacterial cells and microbial exopolymeric substances (EPS) (Badaut & Risacher, 1983; Arp *et al.*, 2003; Souza-Egipsy *et al.*, 2005; Benzerara *et al.*, 2010; Cuevas *et al.*, 2011; Bontognali *et al.*, 2014; Burne *et al.*, 2014; Zeyen *et al.*, 2015; Pace *et al.*, 2016; Buey *et al.*, 2018; Kremer *et al.*, 2019; Wen *et al.*, 2020; Lamérand *et al.*, 2022; Suosaari *et al.*, 2022b; Buey *et al.*, 2023; Thomas *et al.*, 2024), in most cases contributing to the structural rigidity and early fossilisation of microbialites. However, the mechanisms associated with the formation of Mg-silicates as loose particulate sediments in present-day, low alkalinity lakes have received less attention. Moreover, despite the progress made in understanding the mechanisms of Mg-silicate–carbonate precipitation using experimental simulations (García-Ruiz, 1998; Lakshtanov & Stipp, 2010; Mercedes-Martín *et al.*, 2016; Tutolo & Tosca, 2018), these mineral associations have been insufficiently investigated under the environmental conditions found in coastal lagoons or transitional saline lakes affected by contrasting abiotic and biotic influences (microbial gels, diatom-sourced silica, marine-type solutes, complex lake–seepage mixing zones, and other factors).

Modern analogue environments offer the possibility to illuminate the understanding of the causal relationships between water chemistry and the early genesis of crystalline Mg-silicates at the sediment–water interface or in early diagenetic environments (Buey *et al.*, 2018; Milesi *et al.*, 2020; Muller *et al.*, 2023). Lake Clifton, a coastal lagoon in Western Australia, is a particularly interesting case study because Mg-silicates have been identified (Caselmann, 2005; Burne *et al.*, 2014) in an environment comprising hypersaline lake waters of circumneutral pH and modest alkalinity (Moore, 1987, 1993; Rosen *et al.*, 1996; Forbes & Vogwill, 2016), differing from the more common scenario in which these minerals are observed in highly alkaline lakes (e.g., Atexac, Quechulac, La Preciosa lake, Great Salt Lake, Mono Lake, Lake Van, and Salar de Llamara; see Souza-Egipsy et al., 2005; Zeyen et al., 2015; Pace et al., 2016; Kremer et al., 2019; Suosaari et al., 2022a).

In this contribution, petrographic analysis, hydrochemical data, and microbial genomic data are integrated with geochemical modelling to reveal the underlying mechanisms responsible for the formation of newly discovered amorphous Mg-silicates in Lake Clifton shoreline sediments. The recent environments of Lake Clifton provide an opportunity to quantify the environmental and microbial metabolic processes underpinning incipient mineral formation and its coexistence with coeval carbonates. Additionally, these settings allow for the evaluation of the preservation potential of biotic and abiotic minerals, and their biogeochemical signatures during early diagenesis in both recent and ancient saline lakes.

2. LAKE CLIFTON SITE DESCRIPTION

2.1. Geology and geomorphology

Lake Clifton (-32.759849, 115.653311) is in the Perth Basin, the southern section of the Swan Coastal Plain, in southwestern Australia (Playford *et al.*, 1976) (Fig. 1). It belongs to the Yalgorup Lakes area (Clifton–Preston Lakeland System), which comprises several lakes and wetlands of the Southwest Coastal Groundwater Area (Playford *et al.*, 1976; Commander, 1988). The Yalgorup Lakes area is bounded by Precambrian basement rocks of the Yilgarn Block to the east and Indian Ocean to the west, and its physiography is dominated by dunes lying parallel to the present coastline (Playford *et al.*, 1976; Moore, 1987; Commander, 1988). Lake Clifton is situated between the Spearwood and Quindalup dune systems to the west, and Bassendean dune system to the east, which comprise low hills and ridges ranging in height from 30 to 70 m above sea level (Commander, 1988; Deeney, 1989).

The dunes are composed of Pleistocene Tamala Limestone and Bassendean Sand, as well as Holocene Safety Bay Sand, which together crop out along the shores of the Clifton–Preston Lakeland System (Playford *et al.*, 1976; Commander, 1988; Deeney, 1989). These Quaternary units unconformably overlie the sedimentary rocks of the buried Cretaceous Leederville Formation, which mainly consists of sands, siltstones, and glauconitic shales (Commander, 1988; Deeney, 1989). The Tamala Limestone comprises calcareous aeolianite of marine to lacustrine sediments made up of quartz sands, shell fragments, and shell beds, suggesting deposition in coastal dune environments (McArthur & Bartle, 1980; Commander, 1988). The unit exhibits calcrete and karstified horizons, calcified plant roots, and solution pipes (Lipar & Webb, 2015). The Bassendean Sand (Playford & Low, 1971) consists of white to pale grey, moderately sorted, fine- to medium-grained quartz sand of aeolian origin, which forms a thin cover over much of the coastal plain east of Lake Clifton. The Safety Bay Sand unit (Playford *et al.*, 1976) comprises unlithified quartzose calcarenites deposited in the Quindalup Dune System, overlying the Tamala Limestone in a strip as much as 1 km wide along the coast and reaching a thickness of 50 m (Commander, 1988).

2.2. Hydrogeology

The surface sedimentary units surrounding the Clifton–Preston Lakeland System are hydraulically connected to form an unconfined aquifer, which can be subdivided into different flow systems depending on water-table configuration, salinity contrasts, and geology (**Fig. 1**) (Commander, 1988; Deeney, 1989). The Myalup flow system enters Lake Clifton to the west, the Harvey estuary and its river to the northeast, and the Collie River to the south (Commander, 1988; Deeney, 1989), and the dynamics of discharge from this flow system into the lake strongly influence the water composition (**Fig. 1A**) (Moore, 1987; Rosen *et al.*, 1996). Myalup water comprises a brackish mixture of meteoric, estuarine, saline, and hypersaline groundwaters, and flows towards Lake Clifton under a very low hydraulic gradient (Moore, 1987; Commander, 1988; Forbes & Vogwill, 2016). A combination of long-term reduction in rainfall, high evaporation, and groundwater abstraction owing to anthropogenic activities has increased the salinity of Lake Clifton in recent decades (Knott *et al.*, 2003; Smith *et al.*, 2010; Forbes & Vogwill, 2016). Thus, Lake Clifton is now predominantly a hypersaline evaporative lake punctuated by periods of hyposaline conditions when rainfall exceeds evaporation (Moore, 1987; Forbes & Vogwill, 2016). The dynamic position of the water table may indicate that potential groundwater leakage exists to the underlying sediments of the Leederville Formation (**Fig. 1A-B**) (Commander, 1988).

2.3. Lake-water chemistry

Lake-water composition has fluctuated in recent decades because of changes in hydrological balance (rainfall, evaporation, and groundwater fluxes). In the 1980s and 1990s, salinity ranged between 17 g/L and 31.5 g/L (Moore & Turner, 1988; Rosen *et al.*, 1996; Chagas *et al.*, 2016), reaching values as high as 32.2 g/L over the period 2001–2005 (Smith *et al.*, 2010), and rising to 70 g/L in 2010 (Forbes & Vogwill, 2016). Sodium and chloride are the most abundant ions in both the lake water and upper hyposaline groundwater lens. Cation and anion dominance is Na > Mg > Ca > K, and Cl > SO_4 > HCO_3, respectively, for the lake waters, and these patterns are maintained throughout the year despite seasonal fluctuations (Moore, 1987; Rosen *et al.*, 1996; Chagas *et al.*, 2016; Forbes & Vogwill, 2016). The groundwater flowing into the lake displays a cationic order of abundance of Na > Ca > Mg > K, and anionic order of Cl > HCO_3 > SO_4 (Moore, 1987; Rosen *et al.*, 1996; Forbes & Vogwill, 2016). Relative to seawater, Lake Clifton is enriched in SiO_2, but depleted in Sr, Mn, and Br (Rosen *et al.*, 1996). The pH values in the lake are slightly alkaline (8.5) to neutral (7) coinciding with the periods of highest and lowest lake-water levels, respectively (Forbes & Vogwill, 2016).

2.4. Climate

The climate of the region is Mediterranean with hot summers, and dry and cool winters. Rainfall data have a seasonal component, with higher values between March and September, and a maximum between May and July (Moore, 1987; Rosen *et al.*, 1996; Forbes & Vogwill, 2016). According to the Bureau of Meteorology (e.g., boreholes #61319530 and #61319505), rainfall intensities have been decreasing in recent decades. Annual evaporation rates at Lake Clifton (1369 mm) have historically been close to twice the average annual precipitation (762 mm) (Moore, 1987; Rosen et al., 1996).

2.5. Microbialites and microbial composition

Lake Clifton is characterised by the occurrence of microbialites (Burne & Moore, 1987; Moore, 1993) living in association with lakebed sediments and extending along the eastern and northwestern margins of the lake (Moore & Burne, 1994). These are dominated by thrombolites with coarsely laminated microstructures and mesoclotted fabrics (Kennard & James, 1986; Moore, 1993; Moore & Burne, 1994). Thrombolites display an array of external isolated morphologies, growing up to 1.3 m above the lakebed, or are distributed as a belt of coalesced structures that is over 6 km long and up to 120 m wide (Moore, 1987; Moore & Burne, 1994) (**Fig. 1C**). The internal microstructure consists of a mineralised framework of aragonite ($CaCO_3$) and stevensite mesoclots interspersed with cavities filled with detrital sediments (Moore & Burne, 1994; Burne *et al.*, 2014). The near-surface lakebed sediments contain gastropod shells (*Coxiella striatula* and *Potamopyrgus* spp.), ostracods and charophyte remains, *Navicula* and *Tabellaria* diatom frustules (Lluesma-Parellada 2015), debris from thrombolites, and carbonate mud (Moore, 1987; Moore & Burne, 1994; Konishi *et al.*, 2001; Burne *et al.*, 2014). Previous studies noted the abundance of filamentous cyanobacterial structures (e.g., *Scytonema* sp.) in both living thrombolitic mats and in the lithified bodies, supporting the view that biologically influenced processes are involved in thrombolite mesoclot development (Moore, 1993; Moore & Burne, 1994). Recent metagenomic analyses have shown a greater abundance of cyanobacteria in thrombolite-associated mats in comparison with non-lithifying microbial mats found amongst sandy sediments, suggesting that photosynthesis plays a major role in mineral formation (Warden *et al.*, 2019). The current prevalence of coccoid cyanobacteria in the lake (Smith *et al.*, 2010), particularly in thrombolite-associated mats, has been associated with an adaptative response to progressively increasing salinity values recorded since 2004 (Warden *et al.*, 2016, 2019).

3. MATERIALS AND METHODS

3.1. Sediment and microbial-mat sample collection

A field survey was performed between July and August 2016 to determine the different Lake Clifton sedimentary environments and collect samples of surface sediments (upper 2 cm), living microbial mats (upper 3 cm), lithified thrombolites (subaerially exposed structures), and lake waters. This sample collection was carried out when the episodically submerged lakebed was subaerially exposed permitting access to the different sub-environments. For clarity, it is here defined living microbial mats as macroscopically layered semi-indurated crusts growing at the interface between water and the upper 2–3 cm-thick layer of loose sediment or forming semi-indurated crusts. Sampling concentrated on two parallel ENE transects: Transect 1, 75.9 m in length (−32.732546, 115.650590), and Transect 2, 89.9 m in length (−32.731309, 115.650132), which traversed the lake shoreline from subaerial to episodically submerged sub-environments (**Figs S1 and S2**). Additional samples were also collected from the northern part of the lake (in the vicinity of −32.717551, 115.639552), north central area (−32.728676, 115.648994), adjacent to Transect 1 (-32.733365, 115.651122), and the boardwalk (−32.745285, 115.654485) (**Figs S1 and S2**).

A total of 63 samples were collected across these localities, including 10 samples of living pustular microbial mats, 16 samples of lakebed sediments, 14 samples formed by non-lithifying microbial sediments, and 25 samples corresponding to lithified thrombolites. Living microbial mats were sampled using sterile gloves and a sterilised stainless-steel spoon that was rinsed with lake water. Subaqueous microbial mats were sampled in glass containers that were filled with lake water from each site. Lakebed sediments were placed in plastic zip-lock bags. Sediment and microbial-mat samples were maintained at 4 °C during transport back to the Geobiology and Geochemistry Laboratory at Vrije Universiteit Amsterdam, The Netherlands. All biological samples were collected under a license from the Department of Parks and Wildlife of Western Australia. The pH and conductivity of the water at each site were measured using a Myron Ultrameter, which was calibrated each morning. Sediment particles were stored in plastic containers that were freeze-dried at Vrije Universiteit Amsterdam Laboratory, The Netherlands. A dyed epoxy resin was added, and bubbles were removed under vacuum. While this method allows for a detailed observation of the sediment features, it could lead to some artifacts, which were considered during the petrographic descriptions. After hardening, the impregnated sediments were made into thin sections for petrographic analysis.

3.2. Microscopic and spectroscopic analysis

Petrography of Lake Clifton bottom sediments was conducted on 59 diamond-polished thin sections using a Nikon Eclipse E400 POL petrographic microscope under plane-polarised and cross-polarised light. Photomicrographs were taken with a Nikon DS-Fi3 camera. High-resolution Field-Emission Scanning Electron Microscopy (FESEM) was used for small-scale microscopic observations on carbon-coated and diamond-polished thin sections using a JEOL

J7100FE instrument operating at 20kV. The JEOL instrument is coupled with silicon drift detectors (SDD) for performing energy-dispersive X-ray spectroscopy (EDS) detectors. Images were obtained using secondary electron (SE) detectors for surface petrography, and backscattered electron (BSE) detectors for chemical information. Maps of Ca, Mg, Si, C, O were obtained using an Oxford Instruments X-Act detector to determine elemental and mineral compositions. Surface and cross-section morphologies were studied using a Tescan Mira 3 SEM operating at 20 kV. Forty-six semi-quantitative elemental analyses were performed via EDS (Oxford Instruments X-max 150 detector) using an accelerating voltage of 20 kV. Mineralogy was studied via X-ray diffraction (XRD; Rigaku SmartLab SE) using a Cu Kα radiation source (lambda = 0.15406 nm) operating at 2 kW and equipped with a Ni CuKβ filter-sample; height alignment was performed before each acquisition. The XRD analyses were supported by molecular data obtained via Fourier Transform Infrared Spectroscopy (FTIR) using an Agilent 4300 instrument in Diamond-ATR configuration. Sample measurements were compiled from three replicates, each comprising 64 scans. Backgrounds were measured for interferometry every 10 minutes and comprised 128 scans.

3.3. Water chemistry

Twenty-one surface water samples from different locations within the lake system were collected for chemical analysis. These included the subaerial zone where groundwater discharged into small pools (labelled as ‘seepage), subaerial–episodically submerged fringe (labelled as ‘beach’), and lake waters in submerged settings (labelled as ‘lake’). Field parameters (temperature, pH, Eh and electric conductivity) were measured at each sampling point. Alkalinity was measured in the field by titration with 0.1N H_2SO_4 to pH values of 4.0. Water samples were filtered with 0.45 and 0.1 µm filters (Millipore), stored in 125 mL polyethylene bottles, acidified to pH < 2 with 1 mL of 5% HNO_3. Samples were stored in a refrigerator before concentrations of major elements were measured within a few days of collection using a Perkin Elmer Optima 5300DV Inductively Coupled Optical Emission Spectrometer (ICP–OES) at the Centre for Microscopy, Characterisation, and Analysis, University of Western Australia (Perth, Australia).

3.4. DNA extraction and sequencing

Ten samples were extracted and analysed for their prokaryotic diversity using 16S rRNA gene sequence library. DNA extraction, amplification, sequencing, and analysis were performed as previously described in Spanning et al. (2022). Briefly, DNA was extracted from the DNeasy Powersoil Kit (Qiagen, Benelux BV) following the provided guidelines. The 16S rRNA gene was amplified using universal primers 8F (5′-AGAGTTTGATYMTGGCTCAG-3′) and 1512R (5′-ACGGYTACCTTGTTACGACTT-3′) (Weisburg *et al.*, 1991) integrating Illumina adapters and 8-nucleotide index barcode sequences (Kozich *et al.*, 2013), purified and sequenced by Macrogen Europe on an Illumina Miseq Platform (Illumina, San Diego, USA). Sequencing reads were grouped in 97% OTUs with USEARCH (Persoon et al., 2017) using the parameters described in Iturbe-Espinoza et al.,(2021). Taxonomic assignment was performed using SILVA v 138.1 (Quast *et al.*, 2013) with Mothur v 1.44.3 (Schloss *et al.*, 2009).

3.5. Visualisation and statistical analysis

Genomic information was analysed using the phyloseq package in R software. Known laboratory contaminants were then removed at the genus level using the reference list provided by Sheik et al., (2018). Organisms known to raise alkalinity by their metabolic activity (Dupraz et al., 2009) were subset as such. Oxygenic phototrophs were subset at the Cyanobacteria phylum level. Anoxygenic phototrophs were subset following the protocol of Hamilton et al.(2019), followed by manual curation at the order and genus level: Chloroflexia, Alphaproteobacteria of the Rhodospirillales and Rhodobacterales orders, and of the *Rhodomicrobium* genus, Bacteroidetes of the Rhodothermales order, and Gammaproteobacteria of the Ectothiorhodospiraceae class and *Halochromatium* genus were kept. Other putative anoxygenic phototrophs, such as members of the Chlorobiota or Gemmatimonadota phyla, were not identified. Sulphate reducers were subset at the order level (Desulfovibrionales, Desulfobacterales, and Desulfuromonadales), family level (Desulfarculaceae), and genus level (*Desulfosporosinus* and *Dethiosulfatibacter*), and pooled altogether. Scripts used for data analysis and visualization are available at the following public repository: https://osf.io/zcywf/, under DOI 10.17605/OSF.IO/ZCYWF.

3.6. Geochemical modelling

Aqueous speciation, water mixing, and mineral equilibria were computed using PHREEQC software, version 3.6.2.15100, release 28.01.2020 (Parkhurst and Appelo, 2013). Saturation indices of solid phases were governed by thermodynamic equilibrium between the minerals and water. The ionic strength of the lake water reached values up to 2.8 times that of standard seawater (Summerhayes and Thorpe, 1996); therefore, the thermodynamic activity coefficients of the aqueous species were calculated with the ion-ion specific interaction parameters included in the Pitzer database. For the case of silica, the interaction parameters were those reported in Azaroual et al.,(1997).

Aragonite, amorphous silica, and several Mg–Si solid phases were included as possible precipitates. The solubility products of sepiolite and kerolite were those reported by Stoessell (1988), and those of aragonite, quartz, and amorphous silica were obtained from the Wateq4f database (Ball and Nordstrom, 1991). The stability of low crystallinity sepiolite (here labelled as sepiolite(d)) was described by Wollast et al. (1968). Although Stoessell (1988) attributed this phase to a lack of solid-solution equilibrium, it is here maintained the stability data as a reference. Some other low crystallinity aluminosilicates might also form but analyses of dissolved aluminium were not available at near neutral pH. To make results closer to field observations (i.e, thickness of sediment layers), the volume of solids obtained by the geochemical simulations will be expressed in mm of mineral thickness per m^2 of lake surface, and m of lake water column, rather than mol/kgw. It is here considered a density of 2.28, 2.31 and 2.15 g/cm^3 for amorphous silica, aragonite and kerolite, respectively.

4. RESULTS

4.1. Lake sub-environments and substrates

The *subaerial environment* was clearly delineated by the abrupt appearance of vegetation (dead tree roots, shrubs, grasses, and charophyte algae), calcareous aeolianite and rhizolith substrates of the Tamala limestone, together with sub-recent vadose lake sediments and weathered thrombolites. This zone was locally pierced by freshwater points sourcing the episodically submerged zone (**Fig. 1C; Figs S1, S2**).

The *episodically submerged environment*, subaerially exposed during the field study, displays different types of substrates: flat-topped and low-lying sand flats, plus shallow water pools and puddles (between 3 and 20 cm in depth, **Figs 1C, 2**).

The *sublacustrine environment* was recognised by permanently submerged locations, with accommodation space progressively increasing offshore allowing the tallest lithified thrombolite buildups to develop (from 20 to 80 cm in height) (**Fig. S1**). In the deeper sublacustrine areas, thrombolites were occasionally covered by soft, green-pigmented microbial mat layers (Moore & Burne, 1994; Warden *et al.*, 2016), which were not observed in the episodically submerged zone (**Fig. 1C**).

Two categories of lakebed substrates were identified according to the degree of lithification, i.e., lithified thrombolites (**Fig. 2A, B**) and soft substrates (pustular microbial mats and non-lithifying microbial sediments) (**Fig. 2B, C**), the latter of which were the focus of this work.

4.1.1. Pustular microbial mats

These mats were whitish to pale ochre coloured, weakly lithified, and display contorted and inflated relief (**Fig. 2B, C**). In cross section, these microbial mats showed different coloured mm-thick layers (orange and green or orange and red, from top to bottom). Internally, they were composed of poorly sorted, irregular aragonite peloid grains and shell debris intermingled with EPS and were preferentially found in exposed sand flats and surrounding lithified thrombolites in the subaerial and episodically submerged zones. Samples RE-LC-5, 36, 49, 50, and 51 belong to this category.

4.1.2. Non-lithifying microbial sediments

These sediments were pale ochre to brownish loose particles that showed different proportions of dark grey–brownish microbial gels either filling the interparticle porosity or sedimented on top of them (**Figs. 2B, D, E; Fig. 3**). These sediments comprised irregular and poorly sorted aragonite peloids, fragments of reworked pustular microbial mats, and minute thrombolite intraclasts (**Fig. 2D, F).** These sediments were either found in exposed low-lying sand flats or at the bottom of shallow-water lake pools and puddles (**Fig. 2A, B, D; Figs S1, S2**). In shallow parts of the sublacustrine zone (‘shelf break’), non-lithifying microbial sediments were concentrated in inter-thrombolite depressions forming straight and sinuous ripple marks (**Fig. 2E**). This investigation focused on the Mg-silicate solids found in microbial sediments of the subaerial and, particularly, the episodically submerged sub-environments (**Figs 3-5**). Samples RE-LC-2, 6, 11, 31, 41, and 44 belong to this category.

4.2. Petrography and mineralogy of lakebed sediments

Compositionally, both pustular microbial mats and non-lithifying microbial sediments from the subaerial and episodically submerged zones comprised a mixture of inorganic and organic constituents that will be described as follows (**Figs 3–6**).

4.2.1. Aragonite peloids

These sediments comprised aragonite peloids displaying a yellowish to dark-brown colour, cloudy to dense appearance, microcrystalline carbonate fabric, and ranging in diameter between 20 µm and 3 mm (**Figs 2F, 3-5**). These grains showed irregular external morphologies and poorly sorted to very poorly sorted depositional textures. Aragonite peloids were the most abundant component in pustular microbial mats and non-lithifying microbial sediments, regardless of the lake environment in which they were found. The only phase identified by XRD was aragonite (**Fig. 6A-B**), although an acid-insoluble residue was found after dissolution in 10% HCl. Analysis of this residue revealed a single phase with a prominent absorption at a wavenumber of 1000 cm^{-1}, which corresponds to the Si–O stretch absorbance. Further absorbance peaks between 1320 cm^{-1} and 1600 cm^{-1} are bending absorbances of Si–O, and a broad absorbance from 2750cm^{-1} to 3750 cm^{-1} corresponds to O–H absorbance in mineralogical formation water (**Fig. 6C-D**). The stoichiometries of the Mg/Si ratio as established by EDS are summarised in **Table S1**.

4.2.2. Mg-silicates and bacterial remains

Amorphous Mg-rich silicate phases occurred as pale green to yellowish, dirty, and loose masses with several hundreds of microns in length, sometimes extending throughout entire thin sections, as interparticle components. They engulfed peloids, often forming floatstone-like textures, but were also present as intraclastic aggregates (**Figs 3–5**). These silicates appeared as cloudy, fine-grained gelatinous substrates localised in close association with a diverse array of organic templates (twisted EPS, clusters of diatom shells, blobs of bacterial filaments, or dark and globular organic-rich remains; **Fig. 3**). Twisted EPS represent dehydrated-looking organic matrices ubiquitous in the thin sections, although their proportions fluctuated largely. Organic templates consisted of flattened particulate material forming a vesicular network of intertwined fibres several hundreds of microns in length, which were coated by Mg-rich silicates(**Fig. 3**). In the more mature cases, the growth of silicate crystals has progressively filled the porosity of these organic structures leaving behind clusters of well-defined elongated silicate aggregates. In other cases, Mg-silicates occurred in association with pennate diatom shells (up to 100 µm in length) that were either found dispersed in the amorphous matrices or forming aggregate bundles of dead skeletons (**Fig. 3B**). In some samples, it was possible to recognise intraclastic blobs containing a mixture of aragonite peloids, diffuse organic remains, and moulds of delicate filamentous cyanobacteria-like structures covered in Mg-silicates (**Fig. 3D**). In addition, dark and dense organic-rich globules occurred ubiquitously, in different proportions in different thin sections, and in association with the aforementioned templates. These Mg–Si materials had consistent stoichiometries (average Mg/Si ratios of 0.66, **Table S1**) like those of the residue from the peloidal samples, they were unrecognisable to XRD analysis, and had consistent IR absorbance behaviour; consequently, they are amorphous kerolite-like materials comparable to that described in Section 4.2.1. previously.

4.2.3. Skeletal grains

Lakebed sediments were also commonly characterised by the occurrence of skeletal debris (between 500µm and 2mm). The most abundant were gastropods *Coxiella striatula* and *Potamopyrgus* spp, and the bivalve *Arthritica semen* that occur in different proportions in all samples as entire or broken specimens (**Fig. 4A**). Also, diatom frustules were found sparsely distributed in the lakebed sediments. Some samples contained fragments of micritised coralline algae, calcified stems and gyrogonites of charophytes, and fragments of vascular plants.

4.3. Microbial communities and their diversity in lakebed sediments

Microbial communities from Mg-silicate-rich sediments were investigated using 16S rRNA gene sequencing. The samples were located in the episodically submerged (samples RE-LC 11, 36, and 41) and subaerial (samples RE-LC 2, 5, 6, 31, 49, 50, and 51; **Figs 1C, 7A**) zones providing an overview of the 15 most represented classes (**Fig. 7B**). Overall, Bacteroidia from the Bacteroidetes phylum dominated all samples with relative abundances ranging from 23%

(sample RE-LC 36) to 75% (sample RE-LC 5). Gammaproteobacteria reached maximum abundances of 23% and 17% in samples RE-LC 50 and RE-LC 51, respectively, dominated by Pseudomonas (8% and 9%, respectively) and Thiotrichaceae (4% and 5%, respectively). Anaerolineae of the Chloroflexi phylum were found in all but sample RE-LC 51, with a maximum total abundance of 20% in sample RE-LC 2. Parcubacteria of the Patescibacteria phylum were found in all samples, with relative abundances as high as 16% and 13% in samples RE-LC 41 and RE-LC 49, respectively.

Phyletic groups known to host photosynthetic organisms (i.e. Cyanobacteria) were found in all samples, with a maximum abundance of ca. 8% in sample RE-LC 41, and minima in samples RE-LC 5, 50, and 51 (0.1%, 0.05%, and 0.03 %, respectively) (**Fig. 7C**). Groups known to host anoxygenic phototrophs were found in all samples except sample 5. They were dominated by members of the Alphaproteobacteria class, including Rhodospirillales (2% relative abundance in sample RE-LC 6, 1.1% in sample RE-LC 36, 0.4% in sample RE-LC 49, and 0.3% in sample RE-LC 31), *Rhodomicrobium* (0.5% in sample RE-LC 11, 0.3% in sample RE-LC 36, 0.2% in sample RE-LC 2, and 0.1% in sample RE-LC 31), Rhodovibrionales (0.9% in sample RE-LC 36), and Rhodobacterales (3% in sample RE-LC 36, and 0.1% in both samples RE-LC 41 and RE-LC 6). The Gammaproteobacteria sequences were affiliated with purple sulphur bacteria Ectothiorhodospiraceae and Halochromatiaceae (1.2% in sample RE-LC 50, 0.6% in sample RE-LC 31, and 0.1 % in sample RE-LC 41). In sample RE-LC 36, Chloroflexia abundance was < 0.1%, and 1% for Bacteroidetes and Rhodothermaceae members. Overall, sample RE-LC 36 had the highest abundance and diversity of anoxygenic phototrophs, with 7.4% of total obtained OTUs potentially linked to this metabolism. Only 0.1% of sequences in sample RE-LC 51 were found to be associated with putative anoxygenic phototrophs (**Fig. 7D**).

Sulphate reducers from Clostridiales and Deltaproteobacteria orders Desulfarculales, Desulfobacterales, Desulfovibrionales, and Desulfuromonadales (**Fig. 7E**) were found in 9 out of 10 samples containing Mg-silicates (no putative sulphate reducers were identified in sample RE-LC 51). Samples RE-LC 2, 11, and 36 had > 5 % of identified OTUs that putatively belonged to sulphate reducing groups (sample RE-LC 2 had over 10%). They were largely dominated by sequences from the Desulfobacterales order, with 2% of Desulfovibrionales-associated sequences for sample RE-LC 36 only. Desulfarculales represented 1% of the 2% of putative sulphate reducers identified in sample RE-LC 50. Samples RE-LC 5, 6, 41, and 49 contained < 1% identified putative sulphate reducers.

4.4. Solution chemistry of sampling sites

The major solutes found in 21 surface waters sampled from subaerial, episodically submerged, and sublacustrine locations (labelled as 'seepage', 'beach', and 'lake' in the field, respectively) are listed in **Table S2**. Solute dominance was Cl > Na > SO_4 > Mg > Ca across the three different settings, consistent with previous studies (Moore, 1987; Rosen et al., 1996; Forbes and Vogwill, 2016). Higher average pH values were recorded in beach waters, followed by seepage water, and finally the lake waters (**Fig. 8**, **Table S2**). Higher average alkalinity and Si concentrations were recorded in seepage waters, while higher Ca, Mg, K, SO_4, Na and Cl concentrations occurred in lake waters (**Fig. 8**). Beach waters show higher supersaturation (positive saturation indices) with respect to authigenic aragonite (0.85–0.96) and Mg-silicate phases such as sepiolite (1.13–1.10) and kerolite (1.77–1.80), with seepage and lake waters having lower saturation conditions for all these minerals (**Table S3**).

5. DISCUSSION

5.1. Geochemical trends of Lake Clifton waters

The analyses of Cl, Na, and Mg obtained from lake waters suggest that a conservative mixing occurred between diluted seepage, and evaporated seawater present in the lake by the time that sampling took place (**Fig. 8A, B; Fig. 9**). Correlation plots for Ca, SO_4, and K (not shown) display the same pattern. Despite the massive precipitation of aragonite as peloids, Ca analysis also revealed a conservative mixing process because aragonite formation is controlled by alkalinity availability, which molarity is lower than that of Ca by one order of magnitude. However, the Si concentrations in beach waters are distinctly lower than those expected from a conservative mixing process (**Fig. 8C, 9**). This behaviour suggests that Si is depleted by the precipitation of a solid phase where Si is the limiting component; this could be either Mg-silicate minerals or diatom shells. Finally, the low pH values measured in the lake samples (near neutral pH in a marine setting) could be caused by the combined effect of evaporation and aragonite precipitation (**Fig. 8D, 9**). Although called "seepage water", the samples labelled under this end member are themselves mixtures of a continental diluted water and marine water, as evidenced by their concentrations of typically marine-sourced solutes. Hence, they probably belong to the continental–marine subsurface mixing zone (Commander, 1988) **(Fig. 1B)**.

5.2. Role of water mixing in the formation of Lake Clifton solid phases

Water samples from the subaerial, episodically submerged, and sublacustrine lake areas showed near-equilibrium or slight supersaturation with respect to aragonite, which is consistent with the widespread observation of aragonite peloids forming the lakebed sediments (**Table S3**, **Figs 2–5**), and constitute the thrombolite build-ups (Moore & Burne, 1994; Caselmann, 2005; Burne *et al.*, 2014; Chagas *et al.*, 2016). However, all water analyses showed undersaturation in amorphous silica and supersaturation with respect to crystalline quartz (**Table S3**, **Fig. 10**), suggesting that the silica concentration of the sublacustrine lake water is probably controlled by the precipitation of other solid phases such as Mg-silicate minerals (Burne *et al.*, 2014) or diatom frustules (Moore & Burne, 1994).

As shown in **Fig. 10**, both subaerial (seepage) and sublacustrine (lake) waters appear to be undersaturated with respect to both kerolite and crystalline sepiolite. Conversely, most of the episodically submerged mixing waters (beach) appear to be in equilibrium or supersaturated with respect to kerolite and crystalline sepiolite, so the formation of these minerals is only thermodynamically possible in these areas. This unique characteristic of the episodically submerged zone arises from three factors: first, the mixing of Mg-rich lake water (**Fig. 8B and 9**) with Si-rich seepage water (**Fig 8C and 9**), second, shallow depth CO_2 degassing to the atmosphere; and third, the location of a maximum of alkalinity-producing microorganisms in this specific setting (**Fig. 7**).

The lack of X-ray scatter in the Mg–Si phase found in Lake Clifton sediments indicates that the material is amorphous (**Fig. 6**), and the Mg:Si stoichiometry obtained from EDS analysis is closer to 3:4 (kerolite) than 3:2 (sepiolite). This specific Mg:Si stoichiometry could simply reflect the relative lack of SiO_2 with respect to Mg as confirmed by the plots of **Fig. 8C**. Consequently, this Mg–Si silicate was considered as an ‘amorphous kerolite-like phase’ for the purpose of the present work.

Experimental synthesis shows that the homogeneous nucleation of amorphous kerolite-like phases is expected to occur in aqueous solutions with alkaline pH, relatively high Mg/Si concentrations, and low to high salinities (Tosca & Masterson, 2014). This is also observed in environments where rapid changes in water chemistry produce significant increases in saturation state, enabling the homogeneous nucleation of kerolite and sepiolite (Tosca, 2015; Pozo & Calvo, 2018). Thus, in arid to semi-arid environments, high supersaturation levels during periods of enhanced evaporation may effectively trigger the nucleation of Mg-silicates from solution as has been suggested for Lake Chad, Lake Yoa, and the Bolivian salars (Gac *et al.*, 1977; Darragi & Tardy, 1987; Bentz & Peterson, 2020). However, while the episodically submerged waters at Lake Clifton record high Mg/Si ratios and high salinities, the pH values of the mixing waters are generally below 8 (**Table S2**). Thus, the formation of Lake Clifton's amorphous kerolite-like precipitates may reflect this relatively circumneutral condition.

Given the relatively low pH and seemingly marginal conditions for homogeneous nucleation, the presence of a pre-existing solid substrate may be needed to minimise the nucleation energy barriers for kerolite-like phases to grow from a slightly supersaturated aqueous phase (Tosca, 2015). Observations indicate the occurrence of poorly hydrated amorphous Mg-silicates in close association with organic debris, including twisted EPS, clusters of diatom shells, blobs of bacterial filaments, and/or dark organic-rich remains (**Figs 3–5**). As documented in many natural systems, the presence of foreign substrates of either biological remains, siliceous material, or detrital clays (Tosca, 2015; Pozo & Calvo, 2018) can lower the interfacial energy required for the heterogeneous mineral nucleation of Mg-silicates and carbonates (Sánchez-Román *et al.*, 2008, 2011, 2023; Cuevas *et al.*, 2011; Krause *et al.*, 2012; Bontognali *et al.*, 2014; Zeyen *et al.*, 2015; Buey *et al.*, 2021, 2023). Thus, it is very likely that the cation binding capacity of the microbial EPS (including diatoms) accumulated in lake sediments facilitates the lowering of supersaturation levels required for the nucleation of Mg-silicates. This spatial correlation and involvement of microbial processes in Mg–Si precipitation has previously been postulated in association with thrombolite mineralization, although in that case it was as stevensite (Burne *et al.*, 2014) .

To test the feasibility of kerolite formation owing to *mixing of lake with seepage waters* in the episodically submerged zone, geochemical modelling was performed assuming heterogeneous precipitation of pure crystalline solid phases as soon as supersaturation was reached (i.e. assumption of no kinetic barriers). Due to the lack of thermodynamic data for the amorphous kerolite-like Mg-Si phases, crystalline kerolite has been used as an approach in the simulations. Calculations simulated the discharge of seepage water (sample 25, the lowest Cl–Na concentration in **Table S2**) into lake water (sample 7, the highest Cl–Na concentration).

Several processes can take place simultaneously when seepage water mix with lake water in the beach: CO_2 degassing, microbially-mediated reactions, and precipitation of solid phases. These processes will be described separately. Degassing causes the alkalinisation of the water ($HCO_3^- + H^+ = CO_2(g)\uparrow + H_2O$) and the precipitation of solid phases can take place as supersaturation is reached. As an example, **Fig. 11** shows the effect of CO_2 degassing in a mixture 50% of seepage and 50% of lake waters. Similar trends can be observed for other mixing proportions (**Fig. S3A, B**). According to **Fig. 11**, if CO_2 degassing is higher than pCO_2 of 2.4, both aragonite and minor kerolite will precipitate from all the mixture proportions (see an example in **Fig. S4**).

5.3. Role of EPS and microbial metabolism in the formation of Lake Clifton minerals

As described above, petrographic observations revealed an intimate intergrowth of kerolite-like precipitates with EPS. To produce an observable amount of aragonite versus kerolite (following a biologically-induced mineral formation pathway *sensu* Dupraz *et al.*, 2009), as empirically recorded in Lake Clifton surficial sediments, an alkalinity pump is required (Tosca *et al.*, 2011; Zeyen *et al.*, 2015; Pace *et al.*, 2016; Buey *et al.*, 2018, 2021; Lamérand *et al.*, 2022). Metabolic processes commonly known to increase alkalinity include oxygenic and anoxygenic photosynthesis (Visscher & Stolz, 2005; Dupraz *et al.*, 2009; Popall *et al.*, 2020; Robles-Fernández *et al.*, 2022), or aerobic and anaerobic heterotrophs (Visscher & Stolz, 2005; Sánchez-Román *et al.*, 2007; Sánchez-Román *et al.*, 2011; Gallagher *et al.*, 2012; Robles-Fernández *et al.*, 2022), Fe-reducing bacteria (Sánchez-Román *et al.*, 2014) or nitrate reducing bacteria (Sánchez-Román *et al.*, 2015). Metabolisms that consume alkalinity, such as aerobic degradation of organic matter, fermentation, and sulphide oxidation, will reduce the chance to reach carbonate and Mg–Si supersaturation and precipitation (Visscher & Stolz, 2005; Dupraz *et al.*, 2009). The genomic analysis of the sediments permits the identification of putative contributors to the alkalinity increase required to precipitate minerals under the conditions observed in Lake Clifton today. While methanogenic organisms were not observed through 16S rRNA gene sequence library, photosynthetic organisms (from diatoms observed throughout the samples, to Oxyphotobacteria Cyanobacteria identified in all samples except sample RE-LC 50; **Fig. 7**) are major contributors to the alkalinity engine. Several putative anoxygenic photosynthesizers identified through their sequences in samples RE-LC 6, 31, 36, and 50 may also be contributing. Sulphate reducers were also identified in samples RE-LC 2, 11, 31, 36, and 50. Combinations of the metabolic potentials of these organisms are the most likely cause of increased alkalinity in the episodically submerged zone (samples RE-LC 41, 36, and 11), and to a lesser extent in the subaerial zone. Samples RE-LC 5, 49, and 51 tend to have a relatively low number of potential contributors to alkalinity increase based on the genomic study. However, the use of 16S rRNA gene sequences from genomic DNA only provides a semiquantitative view of the presence of certain clades and does not allow quantification of these influences. Targeting functional genes (through dedicated primers or metagenomic analysis) and RNA may provide a more accurate view of the metabolic activity of these communities. Metagenomic approaches have been used previously in the Lake Clifton environment to decipher communities involved in lithifying and non-lithifying sediments (Warden *et al.*, 2016). Lithifying mats forming on top of thrombolites partly emerged at some points, suggesting a sublacustrine to episodically submerged environment. Non-lithifying mats were likely sampled in the episodically submerged zone. These mats showed differences marked by the increased presence of photoautotrophic organisms (ca. 25% on average) and associated genes in the lithifying mats, while non-lithifying sediments had lower Cyanobacteria abundances (ca. 5% on average), and increased abundances of sulphate-reducing organisms (ca. 7%) (Warden *et al.*, 2016), as observed herein in 2 out of 3 of the non-lithifying and Mg-silicate-rich samples in the episodically submerged zone (samples RE-LC 36 and 11).

The effect of photosynthesis in biologically-induced mineral formation is modelled with a simplified reaction ($HCO_3^- + H^+ = CH_2O + O_2(g)\uparrow$) and is depicted in Fig. **12A**. As expected from the reactants, the chemical effect of photosynthesis cannot be distinguished from CO_2

degassing (**Fig. 11**), and it only progresses for water CO_2 partial pressures higher than atmospheric ($10^{-3.5}$ bar). For CO_2 pressures lower than atmospheric, water would dissolve CO_2 from the atmosphere and no net alkalinity would be generated. The bacterial sulphate reduction effect on mineral formation has been also calculated with a simplified reaction ($SO_4^{2-} + 2CH_2O + 2H^+ = 2CO_2(g)\uparrow + H_2S(g)\uparrow + 2H_2O$) and is represented in **Fig. 12B**. Since atmospheric H_2S pressure is very low and only 14% of the initial SO_4 in the mixture has been consumed, the limit of the sulphate reduction would also be the atmospheric CO_2 pressure ($10^{-3.5}$ bar). The amount of kerolite formed in both reactions is equivalent (**Fig**. **12A** and **B**). However, since no HCO_3 is consumed, sulphate reduction results in the formation of more aragonite. According to Fig. **12A** and **B**, in the hypothetical case of no CO_2 diffusion, the total generation of alkalinity of both biological reactions should be kept below 5 mmol/L: further reaction would reach a pH higher that 8 and a CO_2 partial pressure lower than atmospheric.

In summary, besides lake and seepage mixing and CO_2 degassing, the congruent occurrence and activity of bacterial sulphate reducers, diatoms- and Cyanobacteria-powering photosynthesis, and anoxygenic phototrophs may be able to generate alkalinity to contribute significantly to the formation of the kerolite-like/aragonite assemblage in the episodically submerged and subaerial zones.

5.4. Modelling versus natural processes: the limits of equilibrium

Under theoretical equilibrium conditions, rather than indicating the actual formation of solids, the modelling results should be interpreted as their possible precipitation. If precipitation does occur, the volume of formed solid phases would represent be maximum possible. In the following lines, a comparison between theoretical equilibrium conditions and actual data was made.

Unfortunately, no direct measurement of the CO_2 partial pressure reached by CO_2 degassing and/or photosynthesis and sulphate reduction is available. However, an indirect indication is given by the pH of the mixture. Thus, several end-member hypotheses are depicted in **Fig. 13**. Firstly, the precipitation of aragonite with no CO_2 degassing and no biological reactions (kerolite remains undersaturated in these mixtures) leads to pH values lower than 7, distinctly lower than observed (scenario 1). Secondly, CO_2 degassing and/or biological consumption to the atmospheric limit of $10^{-3.5}$ bar together with no solid precipitation results in pH as high as 9 (scenario 2). Thirdly, CO_2 degassing and/or biological reactions to atmospheric values coupled with solid precipitation (scenario 3). Finally, no CO_2 degassing and no biological reactions together with no solid precipitation (scenario 4). As shown in **Fig. 13**, most of the measured pH values plot between the scenarios 3 and 4. The measured pH values lower than scenario 3 suggest that CO_2 degassing and/or biological reactions were not reaching the completion to atmospheric values. On the other hand, the analysed pH values higher than scenario 4 suggest that precipitation of solids was not maximum.

In summary, the analysed pH values are consistent with a scenario of incomplete CO_2 degassing and/or biological reactions, and solid precipitation lower than that predicted as saturation is reached.

5.5. Are Mg-silicates triggered by the dissolution of diatom frustules?

The authigenesis of Mg-silicates on the surface of dead diatom frustules accumulated as loose sediment (Badaut & Risacher, 1983; Bentz & Peterson, 2020; Muller *et al.*, 2023) or as pseudomorphic replacements in diatom-bearing microbialites (Zeyen *et al.*, 2015) has been documented previously in saline, alkaline (pH > 8–9) systems. In these cases, evidence of dissolution and coating/replacement of diatom frustules with a variety of poorly crystallised Mg-Si minerals (stevensite, saponite, and kerolite) has been observed. The factors governing the solubility of biogenic silica after diatom death are multiple, including fluctuations of pH, temperature, salinity, depth of water column, and sedimentation rates, among others (Chan, 1989; Conrad *et al.*, 2007; Loucaides *et al.*, 2012; Bentz & Peterson, 2020). Saline to hypersaline lakes with relatively alkaline pH developed in arid regions with moderate to high lake water temperatures and variable water depths are prone to experience higher rates of silica dissolution. Some examples include the mudflats of the Bolivian Altiplano salars (Bentz & Peterson, 2020) , and the surficial sediments of Lake Alchichica in Mexico (Muller *et al.*, 2023). In some Bolivian salars, Mg-rich fluids may be responsible for the slow leaching of thick diatomaceous muds, providing a source of Si to pore fluids, and encouraging the formation of kerolite and Mg-smectite during periods of enhanced evaporation (Bentz & Peterson, 2020). Moreover, the upper decimetres of the diatomaceous sediment at Lake Alchichica have been documented as undergoing a replacement/pseudomorphic transformation to Al-poor Mg-silicates with a composition corresponding to stevensite (Muller *et al.*, 2023).

Thus, it is pertinent to evaluate the potential role of amorphous silica dissolution/ replacement in Lake Clifton Mg-silicate authigenesis given that lake sediments occur in close association with diatom frustules (**Fig. 3B**) (Moore, 1993; Moore & Burne, 1994; Caselmann, 2005). Because SiO_2 is the limiting reagent in Lake Clifton waters (**Fig. 8C**), the active presence of this component is expected to drastically modify the geochemical system described in previous sections. Indeed, the in excess presence of SiO_2, originating from the dissolution of dead diatom frustules plus seepage water-fed silica, would favour the formation of kerolite-like phases (**Fig. 14**). However, the precipitation of observable amounts of kerolite-like phases within the pH values observed in the episodically submerged lake region (averaging 7.7) also requires the consumption of alkalinity, thereby preventing the formation of aragonite even under the most favourable alkalinity conditions (**Fig**. **14**). Consequently, the observation of ubiquitous aragonite peloids in Lake Clifton sediments questions whether aragonite originated in a scenario dominated by excess silica arising from diatom frustule replacement.

5.6. Role of evaporation in aragonite and Mg-silicate formation

In addition to the effects of lake–seepage water mixing, alkalinity pumping reactions of microbial influence, and silica supplied by seepage and diatom dissolution sources, evaporation could potentially play a role in enhancing the supersaturation of lake waters and triggering the precipitation of Mg-silicates in the episodically submerged pools of Lake Clifton. However, all the analysed waters can be explained as linear mixtures of seepage and lake end members (**Fig. 8A, B**), with no evidence of evaporation paths or evaporitic minerals such as gypsum. Moreover, the evaporation of the most diluted mixtures (80% seepage- 20% lake) would result in pH values decreasing and far below those measured in the field. As a result of pH decrease and amorphous silica precipitation (not represented), kerolite saturation indices decrease and remain negative (**Fig. 15**). As a consequence, evaporation can be ruled out as a process leading to Mg-silicate formation in Lake Clifton.

5.7. Chemical evolution of the Lake Clifton: implications for the formation of Mg-silicates

According to the data available, a clear increase in the lake salinity has been observed over the last four decades (data reported in Moore, 1987; Rosen et al., 1996; Caselmann, 2005; Smith et al., 2020; Forbes & Vogwill, 2016; present study). Salinity has risen from half to more than double that of seawater and is associated with a shift in the major chemistry towards marine solutes (see **Table S4** and **Fig. S6**). According to Forbes and Vogwill (2016), the increase in salinity could be attributed to one or several processes: a decrease in rainfall, increasing groundwater pumping in the recharge area, and infiltration of hypersaline groundwater due to the dewatering of the Dawesville Channel. Alongside the rise in salinity, a systematic decrease in pH from slightly alkaline (8.5 to 8.0) to near neutral pH (7.5) has also been observed in the limited data gathered (**Table S4**). This decrease is attributed to a progressive decline in filamentous cyanobacteria and phytoplankton diversity (Rosen et al., 1996; Smith et al., 2010) (**Fig. 16**).

Superimposed on this decadal trend, there is also a seasonal oscillation, with higher pH in summer (December to February) and lower pH in winter (June to August) (Forbes & Vogwill, 2016). pH values measured in the present work align with those reported by these authors for July-September 2010. This behaviour is linked to the hydrological cycle (Rosen et al., 1996): with a two-month delay, winter rainfall reaches the lake via groundwater, bringing nutrients that promote algae and phytoplankton growth through the warm summer months (Moore & Turner, 1988). During the summer, groundwater discharge drops, and evaporation increases prompting salinization, which is followed by declines in biomass growth during autumn months (Moore & Turner, 1988; Rosen *et al.*, 1996; Forbes & Vogwill, 2016). Consistent with the decadal evolution of the lake, higher pH values are associated with high biological productivity, while lower pH values correspond to rises in salinization and the decline of biological activity (Rosen *et al.*, 1996; Forbes & Vogwill, 2016) (**Fig. 16)**.

Compared with the data collected in the present study, the older Lake Clifton waters show lower CO_2 pressures (closer to atmospheric values) and distinctly higher solid supersaturation values (**Table S5**), making them more prone to forming Mg-silicates and aragonite. Assuming that gas diffusion processes in the recent were similar those of the present day, the key factors in the alkalinisation required for Mg-silicate formation in Lake

Clifton would biologically-induced photosynthesis and sulphate reduction (**Fig. 13**) rather than CO_2 degassing (**Fig. 11**).

5.8. Implications for the environmental interpretation of lacustrine Mg-silicates

The occurrence of Mg-silicates (e.g., kerolite, sepiolite, and stevensite) in lacustrine sedimentary successions can provide valuable insights into past environmental conditions owing to their sensitivity to various hydrochemical parameters (Deocampo, 2004, 2005; Tosca & Masterson, 2014; Tosca & Wright, 2018; Bentz & Peterson, 2020; Gebregiorgis *et al.*, 2020; Chase *et al.*, 2021). Integrating geochemical modelling with laboratory precipitation experiments can illuminate the physico-chemical thresholds of Mg-silicate formation. However, caution is warranted when predicting the behaviour of Mg-silicate–carbonate co-precipitation in both recent and ancient environments. While kerolite-like phases are anticipated at high Mg/Si ratios, high salinities, and moderately high pH (Léveillé *et al.*, 2000; Galán & Pozo, 2011; Tosca & Masterson, 2014; Bentz & Peterson, 2020), the data here presented suggest that such Mg–Si phases can also arise in the mixing zone under extremely high Mg/Si ratios (between 24.6 and 337), marine-like salinities (~0.616 mol/Kg), and near-neutral pH (average of 7.68). Consequently, caution should be taken when presuming that experimentally predicted fluid chemistry promoting Mg-silicate formation precisely mirrors lake biogeochemical conditions in which calcium carbonate precipitation is also facilitated.

The discovery of kerolite-like precipitates in recent Lake Clifton microbial sediments contrasts with the previous identification of massive and crystalline stevensite mineralising cyanobacterial sheaths in adjacent lithified thrombolites (Burne *et al.*, 2014). The fact that different Mg-Si textures with different Mg/Si stoichiometries (**Table S1**) were recognised in the lake sediments suggests that a transformation from amorphous Mg-silicates to crystalline stevensite minerals is currently underway. Such diagenetic transformations could be attributed to the gradual dehydration and desiccation of Mg–Si organic/inorganic gels, a process similarly documented in cave environments and palustrine– lacustrine settings (Pozo & Casas, 1999; Léveillé *et al.*, 2000; Tosca & Wright, 2018) thus informing about diagenetic processes rather than depositional conditions. Evidence for desiccation cracking of Mg-Si phases in Lake Clifton sediments is recognised by the angularity of the intraclastic Mg-Si grains intermingled with peloids (**Fig. 4A**). Dehydration processes are intensified in environments that are episodically submerged, such as the mixing zone at Lake Clifton, which experiences intense evaporation during periods of subaerial exposure (wetting–drying cycles) likely contributing to the early diagenetic transformation to stevensite (Tosca & Wright, 2018) at rates as fast as 2,650 ± 30 yr, which are the age estimates for Lake Clifton thrombolites (Lluesma-Parellada 2015). An early diagenetic origin for Lake Clifton stevensite would raise questions about whether fossil occurrences of lacustrine Mg-silicate minerals can be unambiguously linked to the sort of depositional parameters traditionally attributed to its formation: namely : 1) highly alkaline lake waters ($pH > 9$), 2) supersaturation driven by evaporite concentration, 3) precipitation from 'inorganic' gel-like precursors, or 4) deposition in deeper, low-energy sublittoral areas with no exposure of Mg–Si gels to desiccation (e.g., Pozo & Calvo, 2018; Tosca & Wright, 2018). Differently, present observations highlight that stevensite can arise from amorphous Mg-Si phases: 1) nucleated in mild alkalinity settings, 2) without particularly high evaporitic conditions, 3) associated to abundant 'organic'-like substrates, and 4) deposited in shallow, low-energy beach environments undergoing episodic desiccation and subaerial exposition.

Due to the poor preservation of diatom frustules, microbial fossils, and EPS substrates in deep-time sediments and rocks, inferring the ancient lake biogeochemistry of the Mg-silicate–carbonate system is inherently challenging. Consequently, a case-by-case analysis is recommended when interpreting the depositional and diagenetic conditions that gave rise to ancient lacustrine Mg-silicates, acknowledging that petrographic data alone do not provide direct evidence of lake hydrochemical conditions.

Finally, the process-based simulations here presented enable estimations of the potential thickness of minerals deposited per unit of lake surface area and metre of lake water depth, facilitating borehole or field-scale mineral volume predictions in analogous recent and ancient lacustrine settings.

6. CONCLUSIONS

Analysis of petrographic, hydrochemical, and microbial genomic data from Lake Clifton bottom sediments were combined with geochemical modelling to elucidate the mechanisms driving the formation of aragonite peloids and its interparticle amorphous Mg-silicates (i.e., kerolite-like phases) found in its subaerial and episodically submerged environments. The following conclusions can be drawn:

1. Two processes leading to the formation of kerolite-like solids, and aragonite minerals can occur simultaneously when seepage mixes with lake water in the beach environment: CO_2 degassing and biogenic-mediated reactions (photosynthesis and sulphate reduction). Using geochemical modelling, both CO_2 degassing and photosynthesis are indistinguishable. Geochemical simulations considering solely the pure (abiotic) mixing of lake with seepage waters only explains the neoformation of both aragonite and kerolite-like phases if CO_2 degasification progresses to partial pressures lower than $10^{-2.5}$ bar (Fig. 11).

2. Petrographic data suggest that Mg-silicates are closely associated with twisted microbial (EPS), clusters of diatom shells, blobs of bacterial filaments, or dark and globular organic-rich bacterial remains. Furthermore, petrographical and genomic analyses points to diatom and cyanobacteria-powered photosynthesis, putative anoxygenic photosynthesis, and sulphate reduction as major contributing metabolisms to the alkalinity engine required for Mg-silicate–carbonate biologically-induced co-precipitation. Simulations also show that the addition of alkalinity from photosynthesis and/or sulphate reduction (in excess to 3 mmol/L) are needed to form the aragonite/kerolite-like phases assemblage observed in Lake Clifton sediments (assuming no CO_2 diffusion or only very slow diffusion).

3. According to the data available, a clear increase in salinity and pH decrease, together with a change in the biota of the Lake Clifton, can be accounted during the last four decades. Within a year, higher pH values occur in early summer (December to February), coinciding with more microbiological productivity. The decrease in pH leads to lower kerolite-like supersaturation. Therefore, although kerolite-like formation is still possible in winter-2016, the conditions were more favourable in the previous decades and during summers. Assuming that gas diffusion does not change significantly in recent years, the decadal evolution of the water indicates that the alkalinisation required to form Mg-silicates in Lake Clifton would be based in biological reactions rather than CO_2 degassing.

4. Geochemical simulations testing the contribution of dead diatom frustule dissolution towards kerolite authigenesis revealed that the precipitation of observable amounts of kerolite within the pH values measured at Lake Clifton would prevent the formation of aragonite, thus refuting a scenario dominated by excess silica. In addition, evaporation-driven alkalinity-rising reactions cannot explain kerolite precipitation, as this process would lead to pH values lower than those observed and increasing kerolite subsaturation.

5. The discovery of kerolite-like Mg-silicate phases in the microbial-bearing sediments of a hypersaline and slightly alkaline coastal lagoon urges a revision of the biogeochemical models of Mg-silicate–carbonate co-precipitation. A holistic evaluation of the Si-cycling–alkalinity–microbial mineralization interactions in recent saline lakes is crucial to illuminate the understanding of the early diagenesis of lacustrine minerals, as some processes and signatures may have encountered incomplete petrographic preservation in ancient systems.

ACKNOWLEDGEMENTS

This work was supported by BP Exploration Co. (Grant reference: GPTL/BPX/MB/NB/89573) and the Dutch Research Council (NWO) Projects GEOBIOCARBON: OCENW.KLEIN.037 and MECA: ENW.GO.001.033. Warm thanks are given to many colleagues at BP's Carbonate Centre of Expertise (London, UK) for fruitful discussions on continental and ‘Pre-salt’ carbonates, offshore Brazil. Special thanks to the Department of Parks and Wildlife of the Government of Western Australia for granting access to the Yalgorup National Park (Lake Clifton, Australia), and their assistance/ advice during fieldwork and sample collection in 2016. Pietro Maiello (Northumbria University) is also thanked for processing and cleaning the XRD data. Bouk Lacet (VU University Amsterdam) is thanked for thin-section preparation and Dr. Javier García Veigas (CCiTUB, Barcelona) for his assistance with FE-SEM analysis. The Authors are indebted to the three reviewers that provided insightful and constructive comments which greatly helped to improve the manuscript. Special thanks go to Associate (Giovanna Della Porta), and Chief Editors (Gabriela Mángano) for their excellent editorial efforts.

FIGURE CAPTIONS

Figure 1. A. Study site, Lake Clifton, Western Australia in aerial form adapted from Google Earth satellite data (December 2016). Map of groundwater flow systems in this setting, including seepage divides (dotted lines), flow lines (arrowed lines), and names of the domains (in red). Grey lines denote water table contours in m above Australian Height Datum. The Myalup flow system includes the Lake Clifton and Preston subsurface areas. **B**. Diagrammatic cross section showing seepage water flows and types of waters, and directions of seepage water flows between continental and oceanic water masses. Dotted red line divides the Leederville Formation below and Quaternary deposits above (modified from Commander 1988). **C**. Google Earth satellite image (December 2016) with exposed whitish thrombolite belts during low tide conditions. Note sublacustrine, episodically submerged, and subaerial areas. Water samples from Transects 1 and 2 are numbered in black. Soft substrate samples are labelled as RE-LC through the profile. See Fig. S1 for location of additional water samples.

Figure 2. Types of substrates in Lake Clifton episodically submerged sub-environments. **A**. Shallow pools and puddles forming between relic thrombolites during low-tide lake conditions. Note the dark brownish microbial gels covering the bottom of the pools. **B**. Subaerially exposed sand flats covered with semi-indurated and contorted pustular microbial mats, and loose non-lithifying microbial sediments with dark grey–brownish microbial gels. **C**. Detail of broken pustular microbial mats showing mm-thick and poorly continuous coloured laminae. **D.** Shallow pools in the episodically submerged lake area with abundant dark grey–brownish microbial gels occurring as gelatinous ellipsoidal boulders (yellow arrows). **E**. Straight and sinuous ripple marks comprising aragonite peloids filling inter-thrombolite depressions. Note the dark-grey microbial soft boulders (yellow arrows). **F**. Scanning Electron Microscopy photomicrograph of poorly sorted, irregular aragonite peloids, which form non-lithified microbial sediments within shallow puddles.

Figure 3. Photomicrographs of non-lithifying microbial sediments after impregnation in dyed blue epoxy resin. **A**. Poorly sorted aragonite peloids (white arrows) embedded in Mg-silicate masses (yellow arrows) forming floatstone-like depositional textures. Fragments of shell debris and thrombolite intraclasts are present. Sample RE-LC 11. **B**. Irregular peloid (white arrow) surrounded by twisted exopolymers (blue arrows) formed by intertwined organic fibres coated by incipient Mg-silicate minerals (yellow arrows). Note the abundance of dispersed pennate diatom frustules forming bundles (red arrows). **C**. Mg-silicate masses (yellow arrows) filling the porosity of organic templates (blue arrow) leaving behind vesicular textures. Note the dark and dense organic-rich globules intermingled with the Mg silicates and aragonite peloids (white arrows). Sample RE-LC 31. **D**. Intraclast blobs (centre) containing a mixture of peloids (white arrow), diffuse black and rounded organic remains, and moulds of delicate filamentous cyanobacteria-like structures covered in Mg-silicates (yellow arrows). Mollusc shell debris is common. Sample RE-LC 44.

Figure 4. Field-Emission Scanning Electron Microscopy photomicrographs of non-lithifying microbial sediments. Sample RE-LC 11. **A**. Aragonite peloids (whitish colour, white arrow) floating in a cloudy, gelatinous to dense fine-grained Mg-silicate matrix (grey colour, yellow arrows) with some Mg-Si angular intraclasts (in), all of them showing a dominance of Mg and Si. Note some foraminifera shells in the top–centre of the image. **B**. Energy-dispersive X-ray spectroscopy measurements from sites shown with white and red asterisks in Fig. 4A.

Figure 5. Field-Emission Scanning Electron Microscopy photomicrographs of non-lithifying microbial sediments. Sample RE-LC-11. **A**. Twisted exopolymers (grey colour, yellow arrows) forming elongated networks of intertwined fibres where incipient Mg-silicates have been identified (see dominance of Mg and Si). Peloids and intraclastic thrombolite fragments are shown in a light-grey colour (white arrow). **B**. Energy-dispersive X-ray spectroscopy measurements from sites shown with white and red asterisks in Fig. 5A.

Figure 6. **A**. Upper line is the X-ray powder diffraction pattern of a representative homogenised sample (RE-LC 35), and peaks below are approximate intensities of a standard sample of pure aragonite. **B**. X-ray powder diffraction pattern of a representative homogenised sample (RE-LC 65) after acid digestion, showing background scatter. Small peaks arise from small masses of aragonite not removed by digestion. **C**. Black line is the ATR-FTIR spectrum for a representative homogenised sample (RE-LC 35). Grey line is RRUFF standard aragonite (https://rruff.info/aragonite/display=default/R040078). **D**. Black line is the ATR-FTIR spectrum for a representative homogenised sample (RE-LC 35) after acid digestion. Grey line is poorly crystalline interstratified kerolite-stevensite (Ureña-Amate *et al.*, 2008).

Figure 7. A. Sublacustrine (left) to subaerial (right) cross section at the Lake Clifton shoreline, on which samples that underwent metabolic analysis are marked. Samples RE-LC 5, 36, 49, 50, and 51 are pustular microbial mats. Samples RE-LC 2, 6, 11, 31, and 41 are non-lithifying microbial sediments. **B**. Microbial composition of samples containing Mg-silicates (based on 16S rRNA gene sequencing). The 15 most abundant classes are displayed and the sum of remaining OTUs are labelled under “Other”. **C**. Classes of Cyanobacteria, among which only the Oxyphotobacteria are confirmed to perform oxygenic photosynthesis. **D**. Anoxygenic phototrophs observed from different phyla. **E**. Sulphate reducers encompassing Deltaproteobacteria and Clostridiales classes.

Figure 8. Correlation plots of the concentrations of Na (**A**), Mg (**B**), Si (**C**), and pH (**D**) with respect to Cl in Lake Clifton waters for three different locations: seepage, beach, and lake. The concentrations of standard seawater (Summerhayes and Thorpe, 1996) are also plotted as solid triangles.

Figure 9. Depositional profile of Lake Clifton sub-environments displaying the location of water samples studied and their major physico-chemical properties.

Figure 10. Activity diagram of the $MgO–SiO_2–H_2O$ system at 25°C including our analytical data and the solubility products of stevensite (Darragi and Tardy, 1987), low crystallinity sepiolite(d) (Wollast et al., 1967), kerolite, sepiolite (Stoessell, 1988), quartz, and amorphous silica (Ball and Nordstrom, 1991).

Figure 11. Thickness of solids formed (in mm of solid/m^2 surface/m of lake water depth) by the mixing of 50% of seepage and 50% of lake water, and CO_2 progressive degassing. The volume of solid was calculated with a density of 2.31 and 2.15 g/cm^3 for aragonite and kerolite, respectively. Note that pCO_2 equals –log CO_2 pressure. Degasification progresses from left to right until it reaches atmospheric values (3.5).

Figure 12. Thickness of solids formed (in mm of solid/m^2 surface/m of lake water depth) due to photosynthesis (**A**), and sulphate reduction (**B**) on a mixture of 50% of seepage and 50% of lake water.

Figure 13. Yellow circles represent beach sample pH’s plotted according to the lake water fraction. The lines depict pH trends according to end-member theoretical scenarios: (1) precipitation of aragonite with no CO_2 degassing (kerolite remains undersaturated in the mixtures); (2) CO_2 degassing to pCO_2 of 3.5 without solid precipitation; (3) CO_2 degassing to CO_2 of 3.5 with solid precipitation; (4) no CO_2 degassing and no mineral precipitation.

Figure 14. Thickness of solids formed (in mm of mineral/m^2 surface/m of lake water depth) by the mixing of 50% of seepage water and 50% of lake water, and adding alkalinity from CO_2 degassing, and microbial photosynthesis, and sulphate reduction. The simulation consider that silica is available from dissolution of dead diatom shells.

Figure 15. Evolution of saturation indices of gypsum and kerolite and pH values for a mixture of 80% of seepage and 20% of lake water that undergo concentration due to evaporation.

Figure 16. Sketches illustrating the decadal and seasonal trends in rainfall intensities, salinity gradients, pH fluctuations, cyanobacterial blooms, and putative Mg-silicate and aragonite precipitation patterns in Lake Clifton, Australia. The arrows indicate higher values. Based on data in Moore & Turner (1988); Rosen et al., (1996); Smith et al.,(2010); Forbes & Vogwill (2016), and herein.

REFERENCES

Arizaleta, M.L., **Nightingale, M.** and **Tutolo, B.M.** (2020) A rate law for sepiolite growth at ambient temperatures and its implications for early lacustrine diagenesis. *Geochim Cosmochim Ac*, **288**, 301–315.

Arp, G., **Reimer, A.** and **Reitner, J.** (2003) Microbialite Formation in Seawater of Increased Alkalinity, Satonda Crater Lake, Indonesia. *J Sediment Res*, **73**, 105–127.

Azaroual, M., **Fouillac, C.** and **Matray, J.M.** (1997) Solubility of silica polymorphs in electrolyte solutions, I. Activity coefficient of aqueous silica from 25° to 250°C, Pitzer's parameterisation. *Chem. Geol.*, **140**, 155–165.

Badaut, D. and **Risacher, F.** (1983) Authigenic smectite on diatom frustules in Bolivian saline lakes. *Geochim Cosmochim Ac*, **47**, 363–375.

Baldermann, A., **Mavromatis, V.**, **Frick, P.M.** and **Dietzel, M.** (2018) Effect of aqueous Si/Mg ratio and pH on the nucleation and growth of sepiolite at 25 °C. *Geochim Cosmochim Ac*, **227**, 211–226.

Bentz, J.L. and **Peterson, R.C.** (2020) The formation of clay minerals in the mudflats of Bolivian salars. *Clay Clay Miner*, **68**, 115–134.

Benzerara, K., **Meibom, A.**, **Gautier, Q.**, **Kamierczak, J.**, **Stolarski, J.**, **Menguy, N.** and **Brown, G.E.** (2010) Nanotextures of aragonite in stromatolites from the quasi-marine Satonda crater lake, Indonesia. In: *Tufas and Speleothems: Unravelling the Microbial and Physical Controls* (Ed. M. Pedley and M. Rogerson), 336, 211–224.

Besselink, R., **Stawski, T.M.**, **Freeman, H.M.**, **Hövelmann, J.**, **Tobler, D.J.** and **Benning, L.G.** (2020) Mechanism of Saponite Crystallization from a Rapidly Formed Amorphous Intermediate. *Cryst Growth Des*, **20**, 3365–3373.

Bontognali, T.R.R., **Martinez-Ruiz, F.**, **McKenzie, J.A.**, **Bahniuk, A.**, **Anjos, S.** and **Vasconcelos, C.** (2014) Smectite synthesis at low temperature and neutral pH in the presence of succinic acid. *Appl Clay Sci*, **101**, 553–557.

Bristow, T.F. and **Milliken, R.E.** (2011) Terrestrial perspective on authigenic clay mineral production in ancient Martian lakes. *Clay Clay Miner*, **59**, 339–358.

Buey, C. de S., **Barrios, M.S.**, **Romero, E.G.** and **Montoya, M.D.** (2000) Mg-Rich Smectite "precursor" Phase in the Tagus Basin, Spain. *Clay Clay Miner*, **48**, 366–373.

Buey, P. del, **Cabestrero, Ó.**, **Arroyo, X.** and **Sanz-Montero, M.E.** (2018) Microbially induced palygorskite-sepiolite authigenesis in modern hypersaline lakes (Central Spain). *Appl Clay Sci*, **160**, 9–21.

Buey, P. del, **Sanz-Montero, M.E.**, **Braissant, O.**, **Cabestrero, Ó.** and **Visscher, P.T.** (2021) The role of microbial extracellular polymeric substances on formation of sulfate minerals and fibrous Mg-clays. *Chem Geol*, **581**, 120403.

Buey, P. del, **Sanz-Montero, M.E.** and **Sánchez-Román, M.** (2023) Bioinduced precipitation of smectites and carbonates in photosynthetic diatom-rich microbial mats: Effect of culture medium. *Appl Clay Sci*, **238**, 106932.

Burne, R.V. and **Moore, L.S.** (1987) Microbialites: Organosedimentary Deposits of Benthic Microbial Communities. *Palaios*, **2**, 241.

Burne, R.V., **Moore, L.S.**, **Christy, A.G.**, **Troitzsch, U.**, **King, P.L.**, **Carnerup, A.M.** and **Hamilton, P.J.** (2014) Stevensite in the modern thrombolites of Lake Clifton, Western Australia: A missing link in microbialite mineralization? *Geology*, **42**, 575–578.

Calvo, J.P., **Blanc-Valleron, M.M.**, **Rodríguez-Arandía, J.P.**, **Rouchy, J.M.** and **Sanz, M.E.** (1999) Authigenic clay minerals in continental evaporitic environments. *Palaeoweathering, Palaeosurfaces and Related Continental Deposits*, 129–151.

Caselmann, M. (2005) Rezente und subfossile Mikrobialithe westaustralischer Salzseen-Recent and subfossil microbialites from west australian salt lakes. PhD Dissertation

Chagas, A.A.P., **Webb, G.E.**, **Burne, R.V.** and **Southam, G.** (2016) Modern lacustrine microbialites: Towards a synthesis of aqueous and carbonate geochemistry and mineralogy. *Earth-sci Rev*, **162**, 338–363.

Chan, S.H. (1989) A review on solubility and polymerization of silica. *Geothermics*, **18**, 49–56.

Chase, J.E., **Arizaleta, M.L.** and **Tutolo, B.M.** (2021) A Series of Data-Driven Hypotheses for Inferring Biogeochemical Conditions in Alkaline Lakes and Their Deposits Based on the Behavior of Mg and SiO2. *Mineral-basel*, **11**, 106.

Commander (1988) Geology and Hydrogeology of the "Superficial formations" and coastal lakes between Harvey and Leschenault Inlets (Lake Clifton Project). *Professional Papers Geological Survey of Western Australia Report 23.*, 98pp.

Conrad, C.F., **Icopini, G.A.**, **Yasuhara, H.**, **Bandstra, J.Z.**, **Brantley, S.L.** and **Heaney, P.J.** (2007) Modeling the kinetics of silica nanocolloid formation and precipitation in geologically relevant aqueous solutions. *Geochim Cosmochim Ac*, **71**, 531–542.

Cuevas, J., **Leguey, S.** and **Ruiz, A.I.** (2011) Chapter 9 Evidence for the Biogenic Origin of Sepiolite. *Dev Clay Sci*, **3**, 219–238.

Darragi, F. and **Tardy, Y.** (1987) Authigenic trioctahedral smectites controlling pH, alkalinity, silica and magnesium concentrations in alkaline lakes. *Chem Geol*, **63**, 59–72.

Deeney, A.C. (1989) Geology and groundwater resources of the superficial formations between Pinjarra and Bunbury, Perth Basin. *Prof. Pap. Geol. Survey. West. Austr.*, **26**, 31–57.

Deocampo, D.M. (2005) Evaporative evolution of surface waters and the role of aqueous CO2 in magnesium silicate precipitation: Lake Eyasi and Ngorongoro Crater, northern Tanzania. *S Afr J Geol*, **108**, 493–504.

Deocampo, D.M. (2004) Authigenic clays in East Africa: Regional trends and paleolimnology at the Plio–Pleistocene boundary, Olduvai Gorge, Tanzania. *J Paleolimnol*, **31**, 1–9.

Deocampo, D.M. and **Jones, B.F.** (2014) Geochemistry of Saline Lakes. Treatise on Geochemistry (Second Edition). 437–469.

Dupraz, C., **Reid, R.P.**, **Braissant, O.**, **Decho, A.W.**, **Norman, R.S.** and **Visscher, P.T.** (2009) Processes of carbonate precipitation in modern microbial mats. *Earth-sci Rev*, **96**, 141–162.

Forbes and **Vogwill, &** (2016) Hydrological change at Lake Clifton, Western Australia – Evidence from hydrographic time series and isotopic data. *Journal of the Royal Society of Western Australia*, **99(2)**, 47–60.

Gac, J.Y., **Droubi, A.**, **Fritz, B.** and **Tardy, Y.** (1977) Geochemical behaviour of silica and magnesium during the evaporation of waters in Chad. *Chem Geol*, **19**, 215–228.

Galán, E. and **Pozo, M.** (2011) Chapter 6 Palygorskite and Sepiolite Deposits in Continental Environments. Description, Genetic Patterns and Sedimentary Settings. *Dev Clay Sci*, **3**, 125–173.

Galan, E. and **Singer, A.** (eds) (2011) Developments in palygorskite-sepiolite research, a new outlook on these nanomaterials. *Elsevier.*

Gallagher, K.L., **Kading, T.J.**, **Braissant, O.**, **Dupraz, C.** and **Visscher, P.T.** (2012) Inside the alkalinity engine: the role of electron donors in the organomineralization potential of sulfate-reducing bacteria. *Geobiology*, **10**, 518–530.

García-Ruiz, J.M. (1998) Carbonate precipitation into alkaline silica-rich environments. *Geology*, **26**, 843–846.

Gebregiorgis, D., **Deocampo, D.M.**, **Longstaffe, F.J.**, **Simpson, A.**, **Ashley, G.M.**, **Beverly, E.J.**, **Delaney, J.S.** and **Cuadros, J.** (2020) Oxygen Isotopes in Authigenic Clay Minerals: Toward Building a Reliable Salinity Proxy. Geophys Res Lett. doi: 10.1029/2019gl085576

Hamilton, T.L., **Bennett, A.C.**, **Murugapiran, S.K.** and **Havig, J.R.** (2019) Anoxygenic Phototrophs Span Geochemical Gradients and Diverse Morphologies in Terrestrial Geothermal Springs. *mSystems*, **4**, e00498-19.

Iturbe-Espinoza, P., **Brandt, B.W.**, **Braster, M.**, **Bonte, M.**, **Brown, D.M.** and **Spanning, R.J.M. van** (2021) Effects of DNA preservation solution and DNA extraction methods on microbial community profiling of soil. *Folia Microbiol.*, **66**, 597–606.

Jones, B. (1986) Clay mineral diagenesis in lacustrine sediments. In: *Studies in Diagenesis*, US Geological Survey Bulletin 1578 (Ed. F.A. Mumpton),

Jones, B.F. and **Galan, E.** (1988) Hydrous Phyllosilicates, (Exclusive of Micas). *Reviews in Mineralogy*, **19**, 631–674.

Kennard, J.M. and **James, N.P.** (1986) Thrombolites and Stromatolites: Two Distinct Types of Microbial Structures. *Palaios*, **1**, 492.

Knott, B., **Bruce, L.**, **Lane, J.**, **Konishi, Y.** and **Burke** (2003) Is the salinity of Lake Clifton (Yalgorup National Park) increasing? *Journal of the Royal Society of Western Australia*, **86**, 119–122.

Konishi, Y., **Prince, J.** and **Knott, B.** (2001) The fauna of thrombolitic microbialites, Lake Clifton, Western Australia. *Hydrobiologia*, **457**, 39–47.

Kozich, J.J., **Westcott, S.L.**, **Baxter, N.T.**, **Highlander, S.K.** and **Schloss, P.D.** (2013) Development of a Dual-Index Sequencing Strategy and Curation Pipeline for Analyzing Amplicon Sequence Data on the MiSeq Illumina Sequencing Platform. *Appl. Environ. Microbiol.*, **79**, 5112–5120.

Krause, S., **Liebetrau, V.**, **Gorb, S.**, **Sánchez-Román, M.**, **McKenzie, J.A.** and **Treude, T.** (2012) Microbial nucleation of Mg-rich dolomite in exopolymeric substances under anoxic modern seawater salinity: New insight into an old enigma. *Geology*, **40**, 587–590.

Kremer, B., **Kaźmierczak, J.** and **Kempe, S.** (2019) Authigenic replacement of cyanobacterially precipitated calcium carbonate by aluminium-silicates in giant microbialites of Lake Van (Turkey). *Sedimentology*, **66**, 285–304.

Lakshtanov, L.Z. and **Stipp, S.L.S.** (2010) Interaction between dissolved silica and calcium carbonate: 1. Spontaneous precipitation of calcium carbonate in the presence of dissolved silica. *Geochim Cosmochim Ac*, **74**, 2655–2664.

Lamérand, C., **Shirokova, L.S.**, **Petit, M.**, **Bénézeth, P.**, **Rols, J.** and **Pokrovsky, O.S.** (2022) Kinetics and mechanisms of cyanobacterially induced precipitation of magnesium silicate. *Geobiology*, **20**, 560–574.

Léveillé, R.J., **Fyfe, W.S.** and **Longstaffe, F.J.** (2000) Unusual Secondary Ca-Mg-Carbonate-Kerolite Deposits in Basaltic Caves, Kauai, Hawaii. *J Geology*, **108**, 613–621.

Lipar, M. and **Webb, J.A.** (2015) The formation of the pinnacle karst in Pleistocene aeolian calcarenites (Tamala Limestone) in southwestern Australia. *Earth-Sci. Rev.*, **140**, 182–202.

Loucaides, S., **Cappellen, P.V.**, **Roubeix, V.**, **Moriceau, B.** and **Ragueneau, O.** (2012) Controls on the Recycling and Preservation of Biogenic Silica from Biomineralization to Burial. *Silicon*, **4**, 7–22.

McArthur, W.M. and **Bartle, G.A.** (1980) Soils and land use planning in the Mandurah-Bunbury coastal zone, Western Australia. *Melbourne, CSIRO*, 14 pp.

Meldrum, F.C. and **Cölfen, H.** (2008) Controlling Mineral Morphologies and Structures in Biological and Synthetic Systems. *Chem Rev*, **108**, 4332–4432.

Mercedes-Martín, R., **Ayora, C.**, **Tritlla, J.** and **Sánchez-Román, M.** (2019) The hydrochemical evolution of alkaline volcanic lakes: a model to understand the South Atlantic Pre-salt mineral assemblages. *Earth-sci Rev*, **198**, 102938.

Mercedes-Martín, R., **Rogerson, M.R.**, **Brasier, A.T.**, **Vonhof, H.B.**, **Prior, T.J.**, **Fellows, S.M.**, **Reijmer, J.J.G.**, **Billing, I.** and **Pedley, H.M.** (2016) Growing spherulitic calcite grains in saline, hyperalkaline lakes: experimental evaluation of the effects of Mg-clays and organic acids. *Sediment Geol*, **335**, 93–102.

Milesi, V.P., **Debure, M.**, **Marty, N.C.M.**, **Capano, M.**, **Jézéquel, D.**, **Steefel, C.**, **Rouchon, V.**, **Albéric, P.**, **Bard, E.**, **Sarazin, G.**, **Guyot, F.**, **Virgone, A.**, **Gaucher, E.C.** and **Ader, M.** (2020) Early Diagenesis of Lacustrine Carbonates in Volcanic Settings: The Role of Magmatic CO2 (Lake Dziani Dzaha, Mayotte, Indian Ocean). *Acs Earth Space Chem*, **4**, 363–378.

Millot, G. (1970) Geology of Clays, Springer: Berlin/Heidelberg, Germany.

Molnár, Z., **Pekker, P.**, **Dódony, I.** and **Pósfai, M.** (2021) Clay minerals affect calcium (magnesium) carbonate precipitation and aging. *Earth Planet Sc Lett*, **567**, 116971.

Moore, L. (1993) The modern microbialites of Lake Clifton, South-Western Australia. PhD Dissertation. University of Western Australia. 266pp.

Moore, L. (1987) Water chemistry of the coastal saline lakes of the Clifton-Preston Lakeland system, south-western Australia, and its influence on stromatolite formation. *Mar Freshwater Res*, **38**, 647–660.

Moore, L. and **Turner, J.** (1988) Stable isotopic, hydrogeochemical and nutrient aspects of lake-groundwater relations at Lake Clifton, Western Australia.pdf. *Proceedings of the Swan Coastal Plain Groundwater Management Conference, Perth*, 252–272.

Moore, L.S. and **Burne, R.V.** (1994) The modern thrombolites of Lake Clifton, Western Australia. In: *Phanerozoic Stromatolites II* (Ed. J. Bertrand-Sarfati and C. Monty), 3–29.

Mulders, J.J.P.A. and **Oelkers, Eric.H.** (2020) An experimental study of sepiolite dissolution rates and mechanisms at 25 °C. *Geochim Cosmochim Ac*, **270**, 296–312.

Muller, E., **Rapin, W.**, **Caumartin, J.**, **Jézéquel, D.**, **Wever, A.D.**, **Thomazo, C.**, **Havas, R.**, **López-García, P.**, **Moreira, D.**, **Tavera, R.** and **Benzerara, K.** (2023) Diagenetic formation of stevensite by replacement of diatom frustules in the sediments of the alkaline Lake Alchichica (Mexico). *Sedimentology*, **70**, 1013–1038.

Pace, A., **Bourillot, R.**, **Bouton, A.**, **Vennin, E.**, **Galaup, S.**, **Bundeleva, I.**, **Patrier, P.**, **Dupraz, C.**, **Thomazo, C.**, **Sansjofre, P.**, **Yokoyama, Y.**, **Franceschi, M.**, **Anguy, Y.**, **Pigot, L.**, **Virgone, A.** and **Visscher, P.T.** (2016) Microbial and diagenetic steps leading to the mineralisation of Great Salt Lake microbialites. *Sci Rep.*, **6**, 31495.

Playford, P.E., **Cockbain, A.E.** and **Low, G.H.** (1976) Geology of the Perth basin, Western Australia. *Geological Survey of Western Australia*, 300 pp.

Playford, P.E. and **Low, G.H.** (1971) Definitions of some new and revised rock units in the Perth Basin. *Western Australia Geological Survey, Annual Report*, 44–46.

Popall, R.M., **Bolhuis, H.**, **Muyzer, G.** and **Sánchez-Román, M.** (2020) Stromatolites as Biosignatures of Atmospheric Oxygenation: Carbonate Biomineralization and UV-C Resilience in a Geitlerinema sp. - Dominated Culture. *Front. Microbiol.*, **11**, 948.

Pozo, M. and **Calvo, J.P.** (2018) An Overview of Authigenic Magnesian Clays. *Minerals*, **8**, 520.

Pozo, M. and **Casas, J.** (1999) Origin of kerolite and associated Mg clays in palustrine-lacustrine environments. The Esquivias deposit (Neogene Madrid Basin, Spain). *Clay Miner*, **34**, 395–418.

Quast, C., **Pruesse, E.**, **Yilmaz, P.**, **Gerken, J.**, **Schweer, T.**, **Yarza, P.**, **Peplies, J.** and **Glöckner, F.O.** (2013) The SILVA ribosomal RNA gene database project: improved data processing and web-based tools. *Nucleic Acids Res.*, **41**, D590–D596.

Robles-Fernández, A., **Areias, C.**, **Daffonchio, D.**, **Vahrenkamp, V.C.** and **Sánchez-Román, M.** (2022) The Role of Microorganisms in the Nucleation of Carbonates, Environmental Implications and Applications. *Minerals*, **12**, 1562.

Rosen, M.R., **Coshell, L.**, **Turner, J.V.** and **Woodbury, R.J.** (1996) Hydrochemistry and nutrient cycling in Yalgorup National Park, Western Australia. *J Hydrol*, **185**, 241–274.

Sánchez-Román, M., **Fernández-Remolar, D.**, **Amils, R.**, **Sánchez-Navas, A.**, **Schmid, T.**, **Martin-Uriz, P.S.**, **Rodríguez, N.**, **McKenzie, J.A.** and **Vasconcelos, C.** (2014) Microbial mediated formation of Fe-carbonate minerals under extreme acidic conditions. *Sci Rep.*, **4**, 4767.

Sánchez-Román, M., **Gibert, L.**, **Martín-Martín, J.D.**, **Zuilen, K. van**, **Pineda-González, V.**, **Vroon, P.** and **Bruggmann, S.** (2023) Sabkha and salina dolomite preserves the biogeochemical conditions of its depositional paleoenvironment. *Geochim. Cosmochim. Acta*, **356**, 66–82.

Sánchez-Román, M., **Puente-Sánchez, F.**, **Parro, V.** and **Amils, R.** (2015) Nucleation of Fe-rich phosphates and carbonates on microbial cells and exopolymeric substances. *Front. Microbiol.*, **6**, 1024.

Sánchez-Román, M., **Rivadeneyra, M.A.**, **Vasconcelos, C.** and **McKenzie, J.A.** (2007) Biomineralization of carbonate and phosphate by moderately halophilic bacteria. *Fems Microbiol Ecol.*, **61**, 273–284.

Sánchez-Román, M., **Romanek, C.S.**, **Fernández-Remolar, D.C.**, **Sánchez-Navas, A.**, **McKenzie, J.A.**, **Pibernat, R.A.** and **Vasconcelos, C.** (2011) Aerobic biomineralization of Mg-rich carbonates: Implications for natural environments. *Chem Geol*, **281**, 143–150.

Sánchez-Román, M., **Vasconcelos, C.**, **Schmid, T.**, **Dittrich, M.**, **McKenzie, J.A.**, **Zenobi, R.** and **Rivadeneyra, M.A.** (2008) Aerobic microbial dolomite at the nanometer scale: Implications for the geologic record. *Geology*, **36**, 879–882.

Schloss, P.D., **Westcott, S.L.**, **Ryabin, T.**, **Hall, J.R.**, **Hartmann, M.**, **Hollister, E.B.**, **Lesniewski, R.A.**, **Oakley, B.B.**, **Parks, D.H.**, **Robinson, C.J.**, **Sahl, J.W.**, **Stres, B.**, **Thallinger, G.G.**, **Horn, D.J.V.** and **Weber, C.F.** (2009) Introducing mothur: open-source, platform-independent, community-supported software for describing and comparing microbial communities. *Appl. Environ. Microbiol.*, **75**, 7537–41.

Sheik, C.S., **Reese, B.K.**, **Twing, K.I.**, **Sylvan, J.B.**, **Grim, S.L.**, **Schrenk, M.O.**, **Sogin, M.L.** and **Colwell, F.S.** (2018) Identification and Removal of Contaminant Sequences From Ribosomal Gene Databases: Lessons From the Census of Deep Life. *Front. Microbiol.*, **9**, 840.

Smith, M.D., **Goater, S.E.**, **Reichwaldt, E.S.**, **Knott, B.** and **Ghadouani, A.** (2010) Effects of recent increases in salinity and nutrient concentrations on the microbialite community of Lake Clifton (Western Australia): are the thrombolites at risk? *Hydrobiologia*, **649**, 207–216.

Souza-Egipsy, V., **Wierzchos, J.**, **Ascaso, C.** and **Nealson, K.H.** (2005) Mg–silica precipitation in fossilization mechanisms of sand tufa endolithic microbial community, Mono Lake (California). *Chem Geol*, **217**, 77–87.

Spanning, R. van, **Guan, Q.**, **Melkonian, C.**, **Gallant, J.**, **Polerecky, L.**, **Flot, J.-F.**, **Brandt, B.W.**, **Braster, M.**, **Espinoza, P.I.**, **Aerts, J.W.**, **Meima-Franke, M.M.**, **Piersma, S.R.**, **Bunduc, C.M.**, **Ummels, R.**, **Pain, A.**, **Fleming, E.J.**, **Wel, N.N. van der**, **Gherman, V.D.**, **Sarbu, S.M.**, **Bodelier, P.L.E.** and **Bitter, W.** (2022) Methanotrophy by a Mycobacterium species that dominates a cave microbial ecosystem. *Nat. Microbiol.*, **7**, 2089–2100.

Stoessell, R.K. (1988) 25°C and 1 atm dissolution experiments of sepiolite and kerolite. *Geochim. Cosmochim. Acta*, **52**, 365–374.

Suosaari, E.P., **Lascu, I.**, **Oehlert, A.M.**, **Parlanti, P.**, **Mugnaioli, E.**, **Gemmi, M.**, **Machabee, P.F.**, **Piggot, A.M.**, **Palma, A.T.** and **Reid, R.P.** (2022a) Authigenic clays as precursors to carbonate precipitation in saline lakes of Salar de Llamara, Northern Chile. *Commun. Earth Environ.*, **3**, 325.

Suosaari, E.P., **Reid, R.P.**, **Mercadier, C.**, **Vitek, B.E.**, **Oehlert, A.M.**, **Stolz, J.F.**, **Giusfredi, P.E.** and **Eberli, G.P.** (2022b) The microbial carbonate factory of Hamelin Pool, Shark Bay, Western Australia. *Sci Rep.*, **12**, 12902.

Thomas, C., **Filella, M.**, **Ionescu, D.**, **Sorieul, S.**, **Pollier, C.G.L.**, **Oehlert, A.M.**, **Zahajská, P.**, **Gedulter, N.**, **Agnon, A.**, **Sanchez, D.F.** and **Ariztegui, D.** (2024) Combined Genomic and Imaging Techniques Show Intense Arsenic Enrichment Caused by Detoxification in a Microbial Mat of the Dead Sea Shore. Geochem, Geophys, Geosystems. doi: 10.1029/2023gc011239

Tosca, N. (2015) Geochemical pathways to Mg-silicate formation. In: *Magnesian Clays: Characterization, Origins and Applications*, 283–329.

Tosca, N.J., **Macdonald, F.A.**, **Strauss, J.V.**, **Johnston, D.T.** and **Knoll, A.H.** (2011) Sedimentary talc in Neoproterozoic carbonate successions. *Earth Planet Sc Lett*, **306**, 11–22.

Tosca, N.J. and **Masterson, A.L.** (2014) Chemical controls on incipient Mg-silicate crystallization at 25°C: Implications for early and late diagenesis. *Clay Miner*, **49**, 165–194.

Tosca, N.J. and **Wright, V.P.** (2018) Diagenetic pathways linked to labile Mg-clays in lacustrine carbonate reservoirs: a model for the origin of secondary porosity in the Cretaceous pre-salt Barra Velha Formation, offshore Brazil. In: *Reservoir Quality of Clastic and Carbonate Rocks: Analysis, Modelling and Prediction* (Ed. P.J. Armitage, A.R. Butcher, J.M. Churchill, A.E. Csoma, C. Hollis, R.H. Lander, J.E. Omma, and J.E. Worden), *The Geological Society of London*, 435, 33–46.

Tutolo, B.M. and **Tosca, N.J.** (2018) Experimental examination of the Mg-silicate-carbonate system at ambient temperature: Implications for alkaline chemical sedimentation and lacustrine carbonate formation. *Geochim Cosmochim Ac*, **225**, 80–101.

Ureña-Amate, M.D., **Socías-Viciana, M.M.**, **González-Pradas, E.**, **Cantos-Molina, A.**, **Villafranca-Sánchez, M.** and **López-Teruel, C.** (2008) Adsorption of chloridazon from aqueous solution on modified kerolite-rich materials. *J. Environ. Sci. Heal., Part B*, **43**, 141–150.

Velde, B. and **Meunier, A.** (2008) The Origin of Clay Minerals in Soils and Weathered Rocks. *Springer-Verlag Berlin Heidelberg*, 406 pp.

Visscher, P.T. and **Stolz, J.F.** (2005) Microbial mats as bioreactors: populations, processes, and products. *Palaeogeogr Palaeoclim Palaeoecol*, **219**, 87–100.

Warden, J.G., **Casaburi, G.**, **Omelon, C.R.**, **Bennett, P.C.**, **Breecker, D.O.** and **Foster, J.S.** (2016) Characterization of Microbial Mat Microbiomes in the Modern Thrombolite Ecosystem of Lake Clifton, Western Australia Using Shotgun Metagenomics. *Front Microbiol*, **7**, 1064.

Warden, J.G., **Coshell, L.**, **Rosen, M.R.**, **Breecker, D.O.**, **Ruthrof, K.X.** and **Omelon, C.R.** (2019) The importance of groundwater flow to the formation of modern thrombolitic microbialites. *Geobiology*, **17**, 536–550.

Weisburg, W.G., **Barns, S.M.**, **Pelletier, D.A.** and **Lane, D.J.** (1991) 16S ribosomal DNA amplification for phylogenetic study. *J. Bacteriol.*, **173**, 697–703.

Wen, Y., **Sánchez-Román, M.**, **Li, Y.**, **Wang, C.**, **Han, Z.**, **Zhang, L.** and **Gao, Y.** (2020) Nucleation and stabilization of Eocene dolomite in evaporative lacustrine deposits from central Tibetan plateau. *Sedimentology*, **67**, 3333–3354.

Zeyen, N., **Benzerara, K.**, **Li, J.**, **Groleau, A.**, **Balan, E.**, **Robert, J.-L.**, **Estève, I.**, **Tavera, R.**, **Moreira, D.** and **López-García, P.** (2015) Formation of low-T hydrated silicates in modern microbialites from Mexico and implications for microbial fossilization. *Frontiers Earth Sci*, **3**, 64.

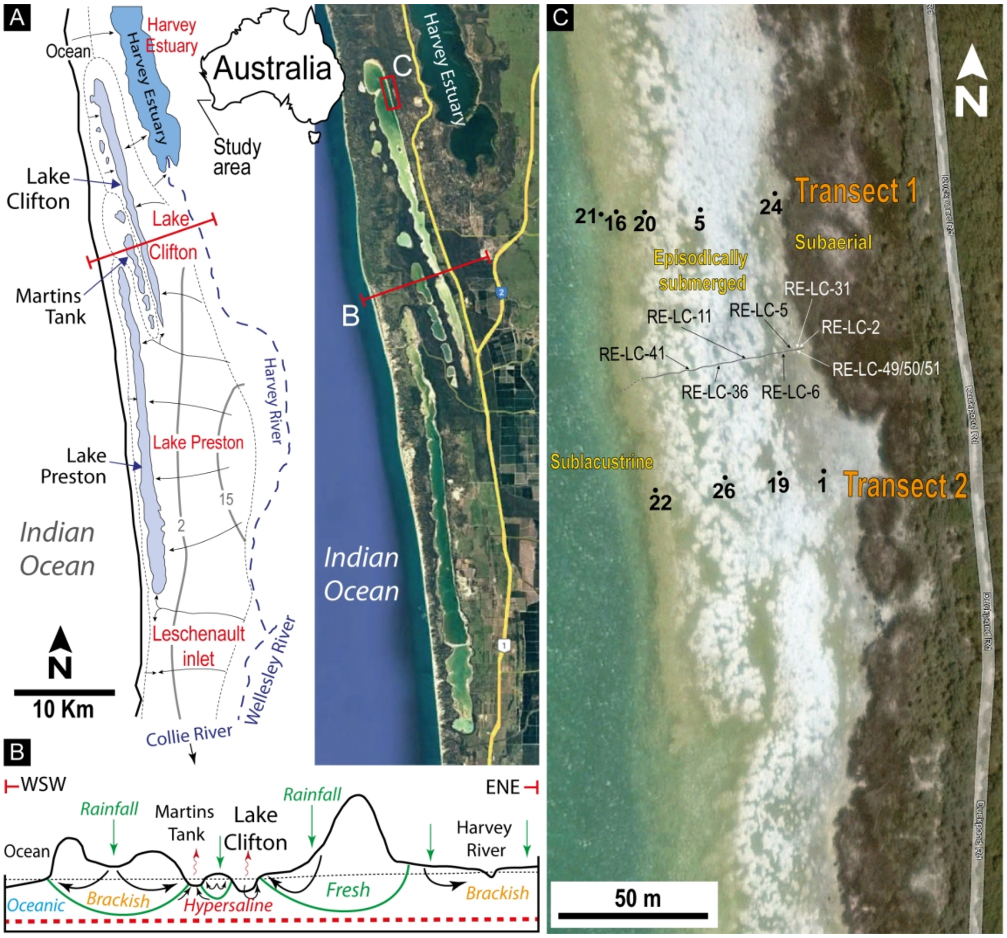

Figure 1. A. Study site, Lake Clifton, Western Australia in aerial form adapted from Google Earth satellite data (December 2016). Map of groundwater flow systems in this setting, including seepage divides (dotted lines), flow lines (arrowed lines), and names of the domains (in red). Grey lines denote water table contours in m above Australian Height Datum. The Myalup flow system includes the Lake Clifton and Preston subsurface areas. B. Diagrammatic cross section showing seepage water flows and types of waters, and directions of seepage water flows between continental and oceanic water masses. Dotted red line divides the Leederville Formation below and Quaternary deposits above (modified from Commander 1988). C. Google Earth satellite image (December 2016) with exposed whitish thrombolite belts during low tide conditions. Note sublacustrine, episodically submerged, and subaerial areas. Water samples from Transects 1 and 2 are numbered in black. Soft substrate samples are labelled as RE-LC through the profile. See Fig. S1 for location of additional water samples.

168x156mm (300 x 300 DPI)

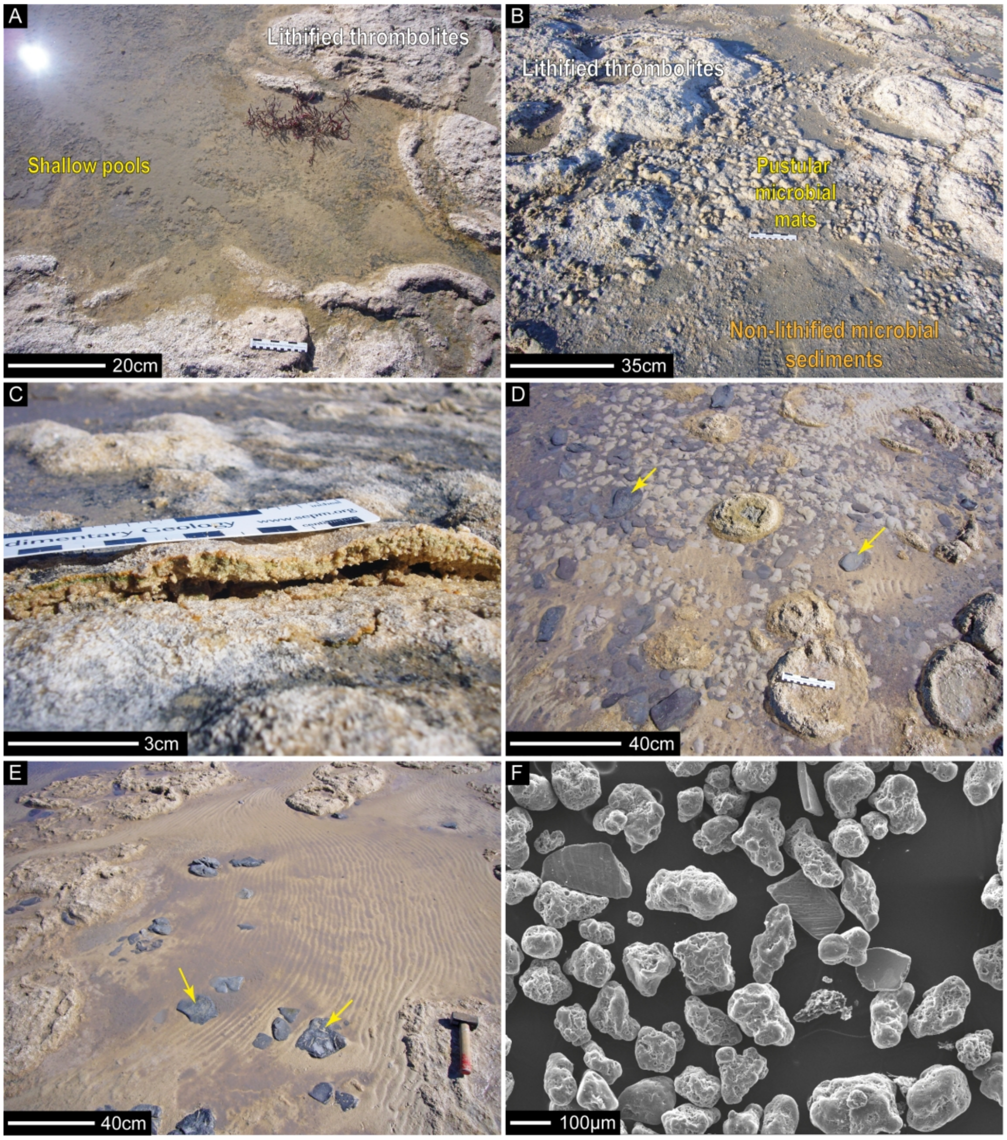

Figure 2. Types of substrates in Lake Clifton episodically submerged sub-environments. A. Shallow pools and puddles forming between relic thrombolites during low-tide lake conditions. Note the dark brownish microbial gels covering the bottom of the pools. B. Subaerially exposed sand flats covered with semi-indurated and contorted pustular microbial mats, and loose non-lithifying microbial sediments with dark grey–brownish microbial gels. C. Detail of broken pustular microbial mats showing mm-thick and poorly continuous coloured laminae. D. Shallow pools in the episodically submerged lake area with abundant dark grey–brownish microbial gels occurring as gelatinous ellipsoidal boulders (yellow arrows). E. Straight and sinuous ripple marks comprising aragonite peloids filling inter-thrombolite depressions. Note the dark-grey microbial soft boulders (yellow arrows). F. Scanning Electron Microscopy photomicrograph of poorly sorted, irregular aragonite peloids, which form non-lithified microbial sediments within shallow puddles.

189x213mm (300 x 300 DPI)

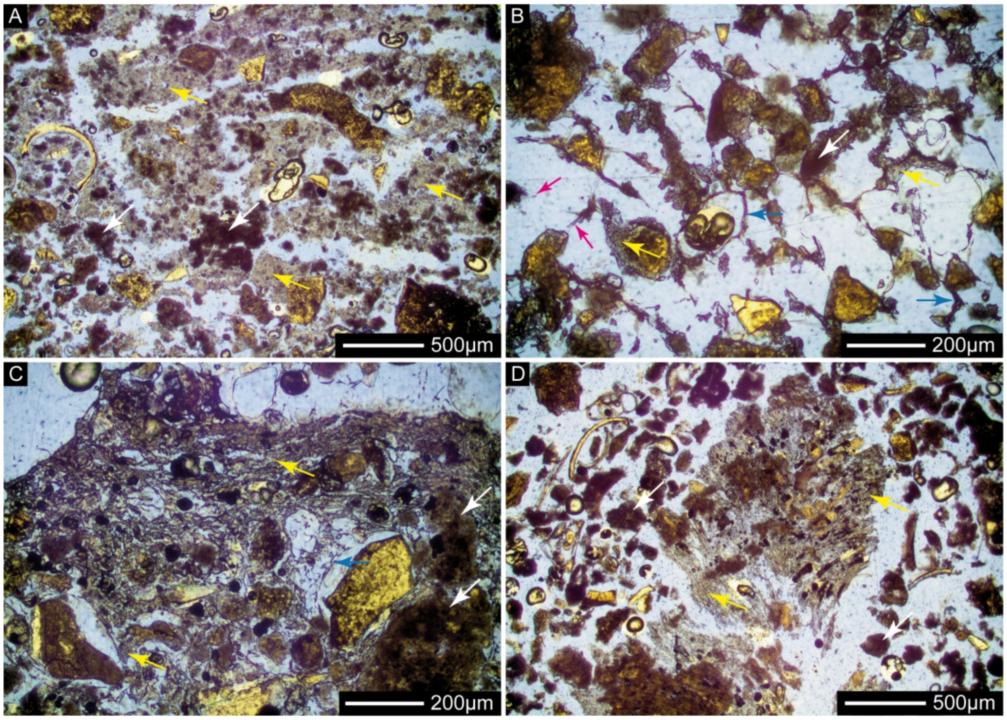

Figure 3. Photomicrographs of non-lithifying microbial sediments after impregnation in dyed blue epoxy resin. A. Poorly sorted aragonite peloids (white arrows) embedded in Mg-silicate masses (yellow arrows) forming floatstone-like depositional textures. Fragments of shell debris and thrombolite intraclasts are present. Sample RE-LC 11. B. Irregular peloid (white arrow) surrounded by twisted exopolymers (blue arrows) formed by intertwined organic fibres coated by incipient Mg-silicate minerals (yellow arrows). Note the abundance of dispersed pennate diatom frustules forming bundles (red arrows). C. Mg-silicate masses (yellow arrows) filling the porosity of organic templates (blue arrow) leaving behind vesicular textures. Note the dark and dense organic-rich globules intermingled with the Mg silicates and aragonite peloids (white arrows). Sample RE-LC 31. D. Intraclast blobs (centre) containing a mixture of peloids (white arrow), diffuse black and rounded organic remains, and moulds of delicate filamentous cyanobacteria-like structures covered in Mg-silicates (yellow arrows). Mollusc shell debris is common. Sample RE-LC 44.

189x134mm (300 x 300 DPI)

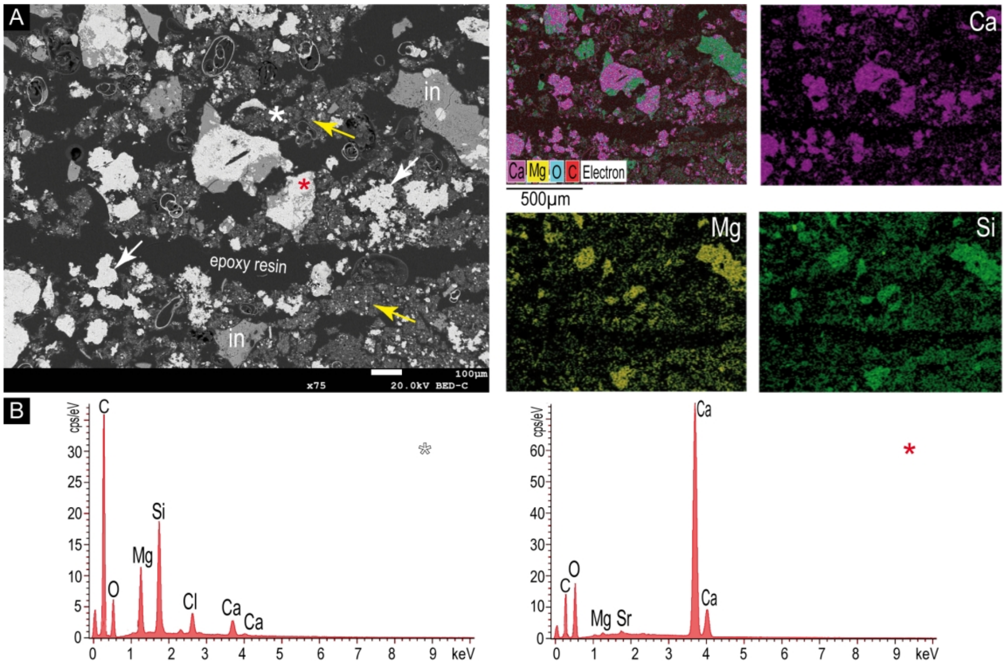

Figure 4. Field-Emission Scanning Electron Microscopy photomicrographs of non-lithifying microbial sediments. Sample RE-LC 11. A. Aragonite peloids (whitish colour, white arrow) floating in a cloudy, gelatinous to dense fine-grained Mg-silicate matrix (grey colour, yellow arrows) with some Mg-Si angular intraclasts (in), all of them showing a dominance of Mg and Si. Note some foraminifera shells in the top–centre of the image. B. Energy-dispersive X-ray spectroscopy measurements from sites shown with white and red asterisks in Fig. 4A.

172x113mm (300 x 300 DPI)

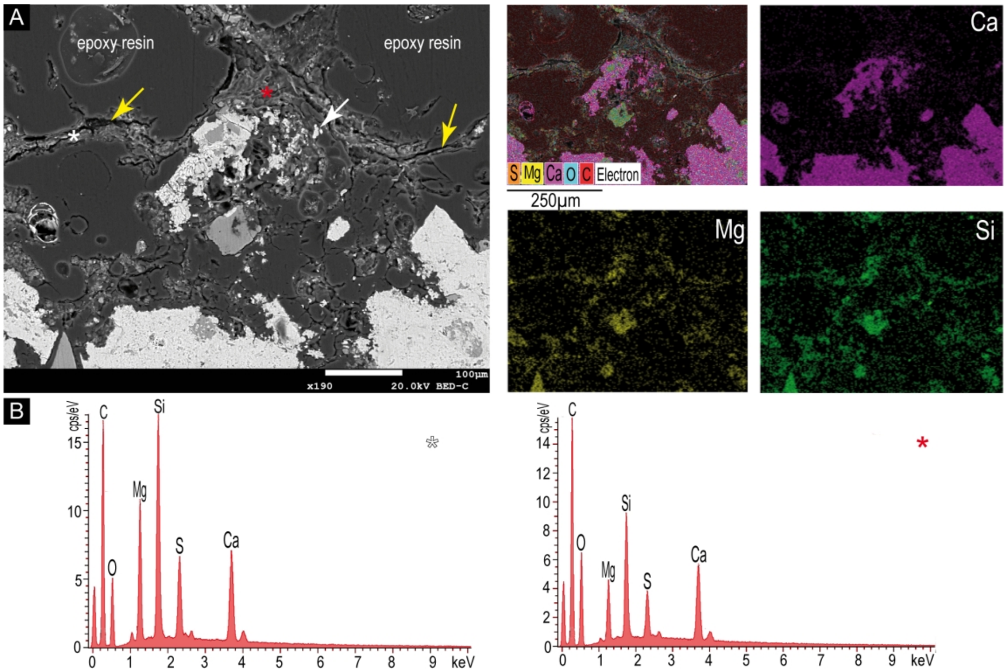

Figure 5. Field-Emission Scanning Electron Microscopy photomicrographs of non-lithifying microbial sediments. Sample RE-LC-11. A. Twisted exopolymers (grey colour, yellow arrows) forming elongated networks of intertwined fibres where incipient Mg-silicates have been identified (see dominance of Mg and Si). Peloids and intraclastic thrombolite fragments are shown in a light-grey colour (white arrow). B. Energy-dispersive X-ray spectroscopy measurements from sites shown with white and red asterisks in Fig. 5A.

171x115mm (300 x 300 DPI)

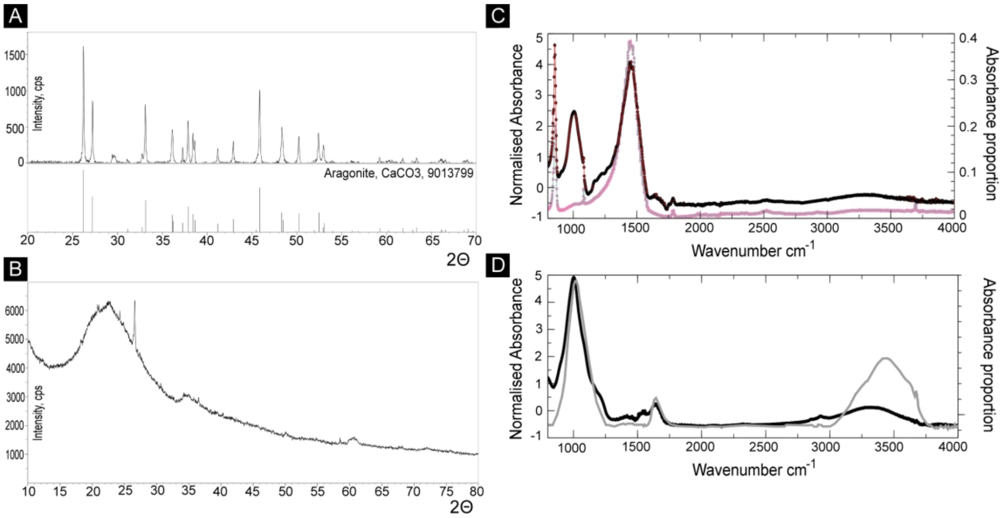

Figure 6. A. Upper line is the X-ray powder diffraction pattern of a representative homogenised sample (RE-LC 35), and peaks below are approximate intensities of a standard sample of pure aragonite. B. X-ray powder diffraction pattern of a representative homogenised sample (RE-LC 65) after acid digestion, showing background scatter. Small peaks arise from small masses of aragonite not removed by digestion. C. Black line is the ATR-FTIR spectrum for a representative homogenised sample (RE-LC 35). Grey line is RRUFF standard aragonite (https://rruff.info/aragonite/display=default/R040078). D. Black line is the ATR-FTIR spectrum for a representative homogenised sample (RE-LC 35) after acid digestion. Grey line is crystalline kerolite (Ureña-Amate et al., 2008).

189x97mm (300 x 300 DPI)

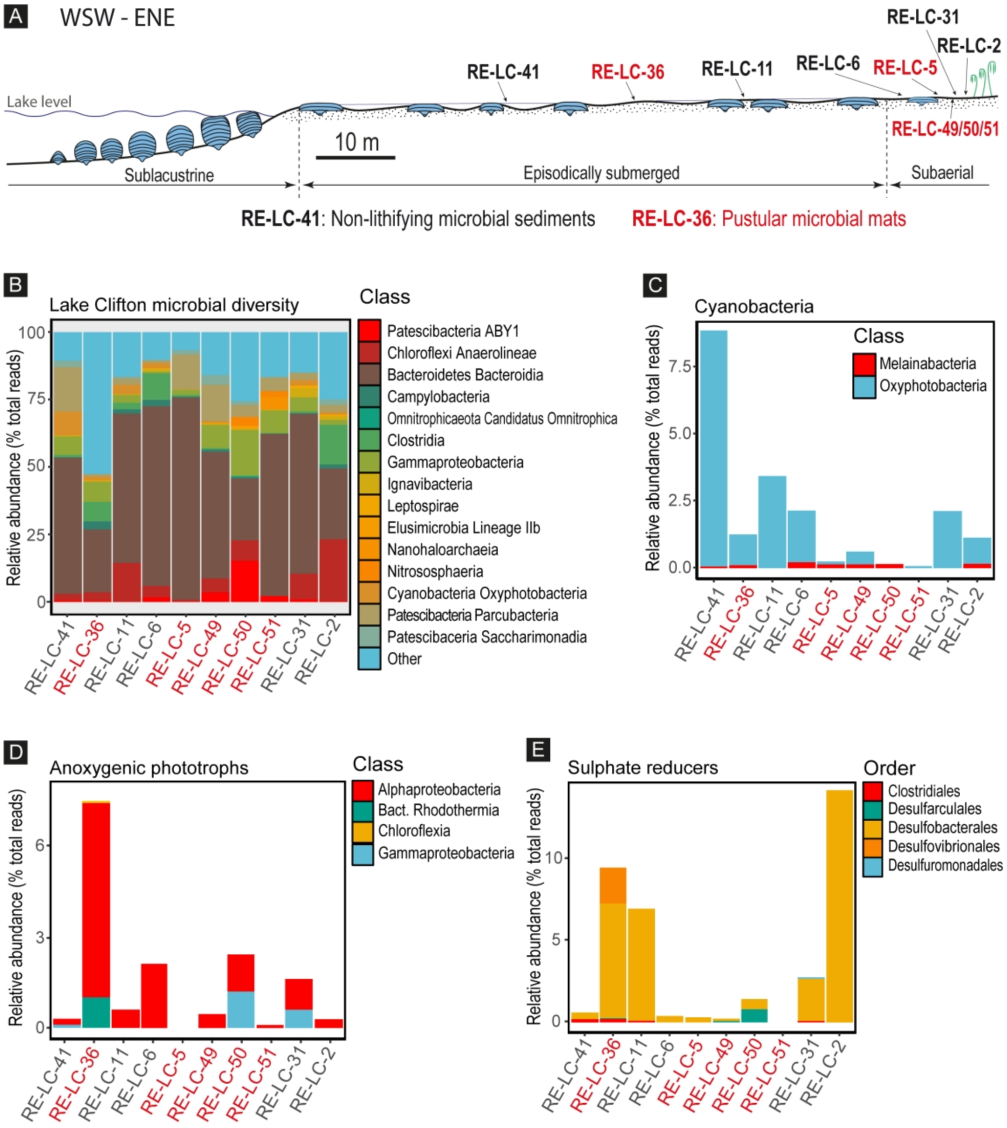

Figure 7. A. Sublacustrine (left) to subaerial (right) cross section at the Lake Clifton shoreline, on which samples that underwent metabolic analysis are marked. Samples RE-LC 5, 36, 49, 50, and 51 are pustular microbial mats. Samples RE-LC 2, 6, 11, 31, and 41 are non-lithifying microbial sediments. B. Microbial composition of samples containing Mg-silicates (based on 16S rRNA gene sequencing). The 15 most abundant classes are displayed and the sum of remaining OTUs are labelled under “Other”. C. Classes of Cyanobacteria, among which only the Oxyphotobacteria are confirmed to perform oxygenic photosynthesis. D. Anoxygenic phototrophs observed from different phyla. E. Sulphate reducers encompassing Deltaproteobacteria and Clostridiales classes.

189x213mm (300 x 300 DPI)

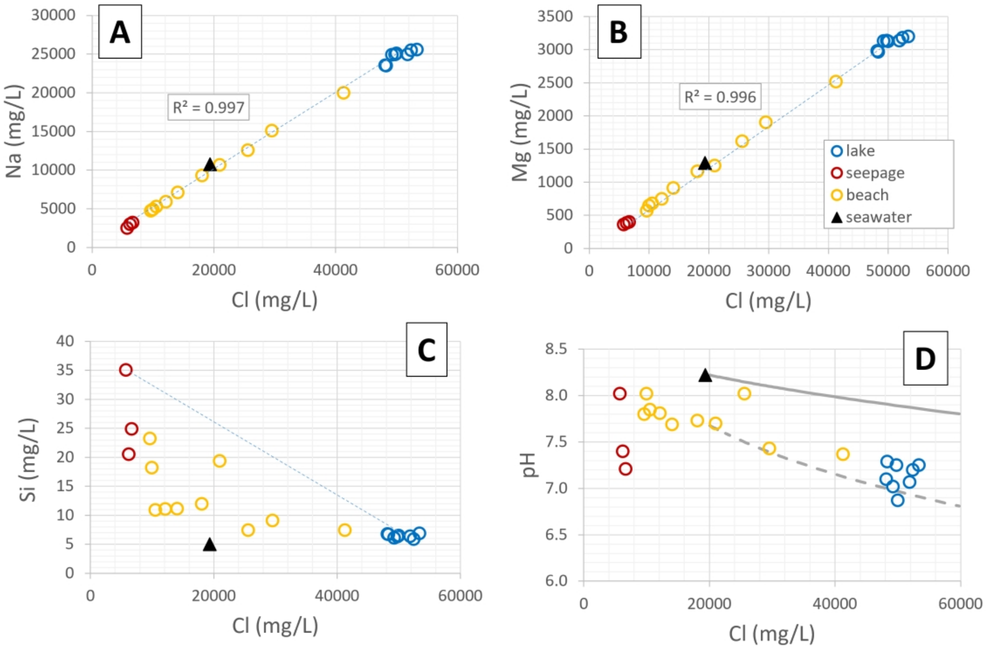

Figure 8. Correlation plots of the concentrations of Na (A), Mg (B), Si (C), and pH (D) with respect to Cl in Lake Clifton waters for three different locations: seepage, beach, and lake. The concentrations of standard seawater (Summerhayes and Thorpe, 1996) are also plotted as solid triangles.

240x157mm (330 x 330 DPI)

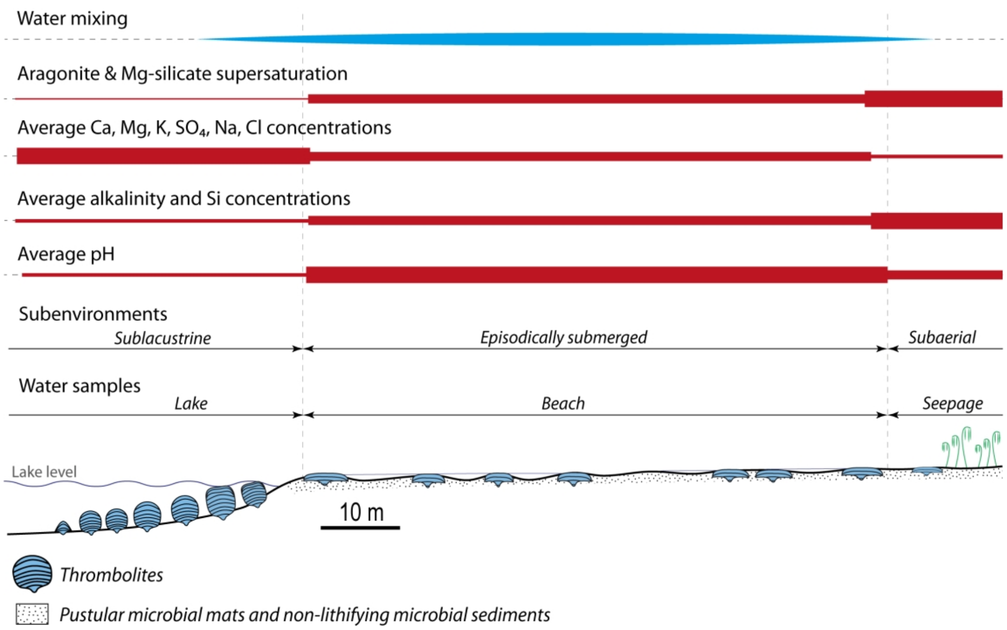

Figure 9. Depositional profile of Lake Clifton sub-environments displaying the location of water samples studied and their major physico-chemical properties.

192x119mm (300 x 300 DPI)

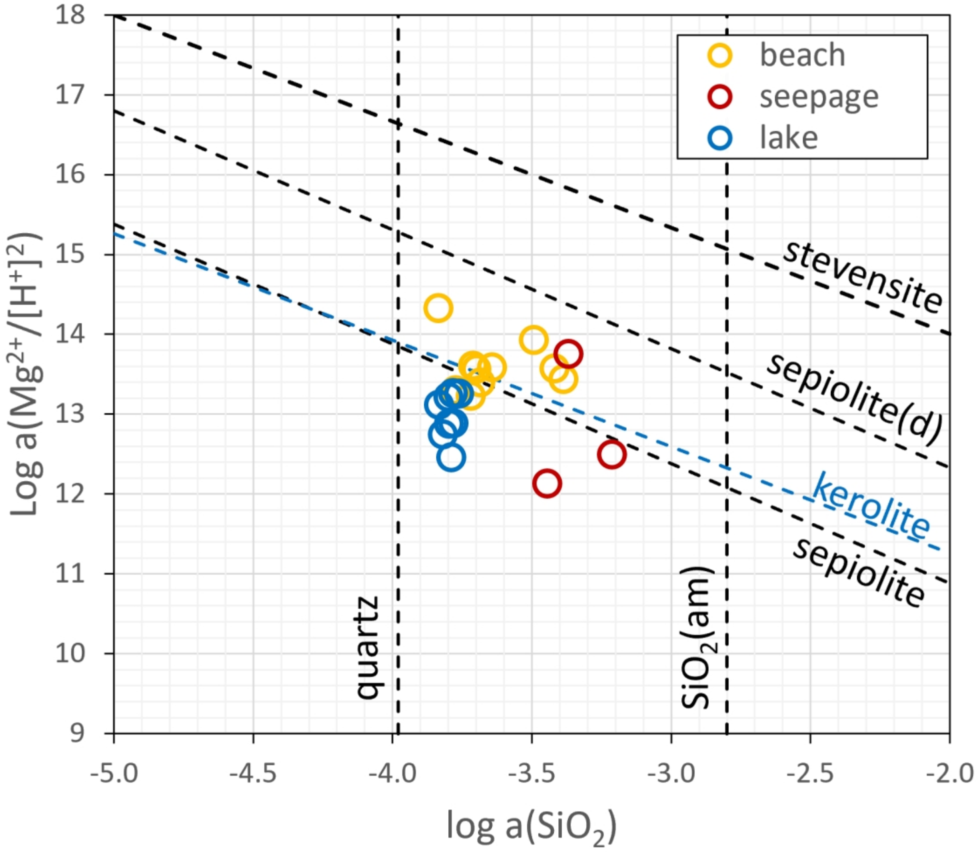

Figure 10. Activity diagram of the MgO–SiO2–H2O system at 25°C including our analytical data and the solubility products of stevensite (Darragi and Tardy, 1987), low crystallinity sepiolite(d) (Wollast et al., 1967), kerolite, sepiolite (Stoessell, 1988), quartz, and amorphous silica (Ball and Nordstrom, 1991).

137x119mm (330 x 330 DPI)

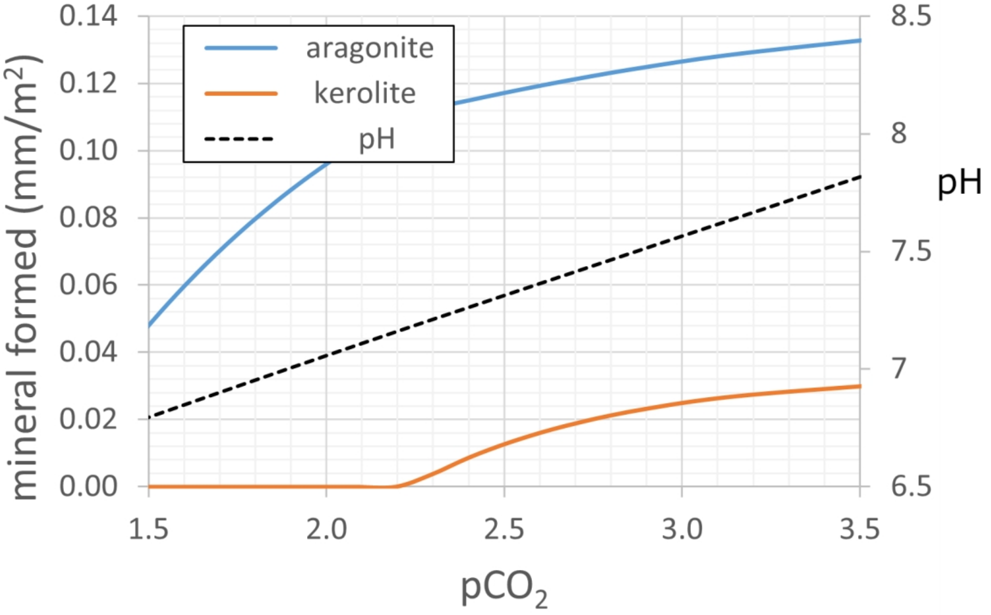

Figure 11. Thickness of solids formed (in mm of solid/m2 surface/m of lake water depth) by the mixing of 50% of seepage and 50% of lake water, and CO2 progressive degassing. The volume of solid was calculated with a density of 2.31 and 2.15 g/cm3 for aragonite and kerolite, respectively. Note that pCO2 equals −log CO2 pressure. Degasification progresses from left to right until it reaches atmospheric values (3.5).

127x81mm (330 x 330 DPI)

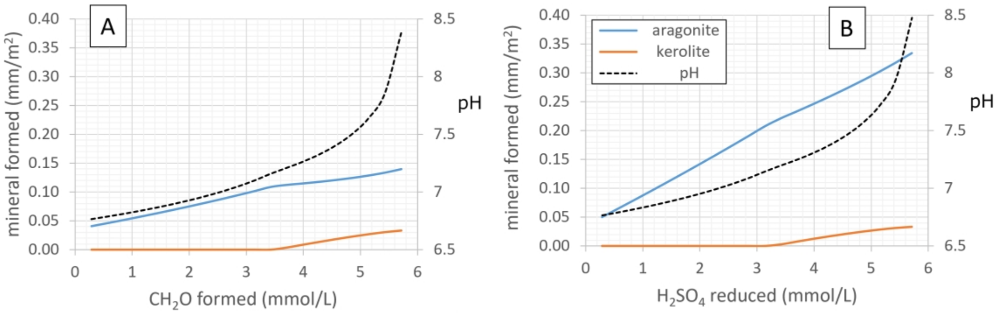

Figure 12. Thickness of solids formed (in mm of solid/m2 surface/m of lake water depth) due to photosynthesis (A), and sulphate reduction (B) on a mixture of 50% of seepage and 50% of lake water.

244x76mm (330 x 330 DPI)

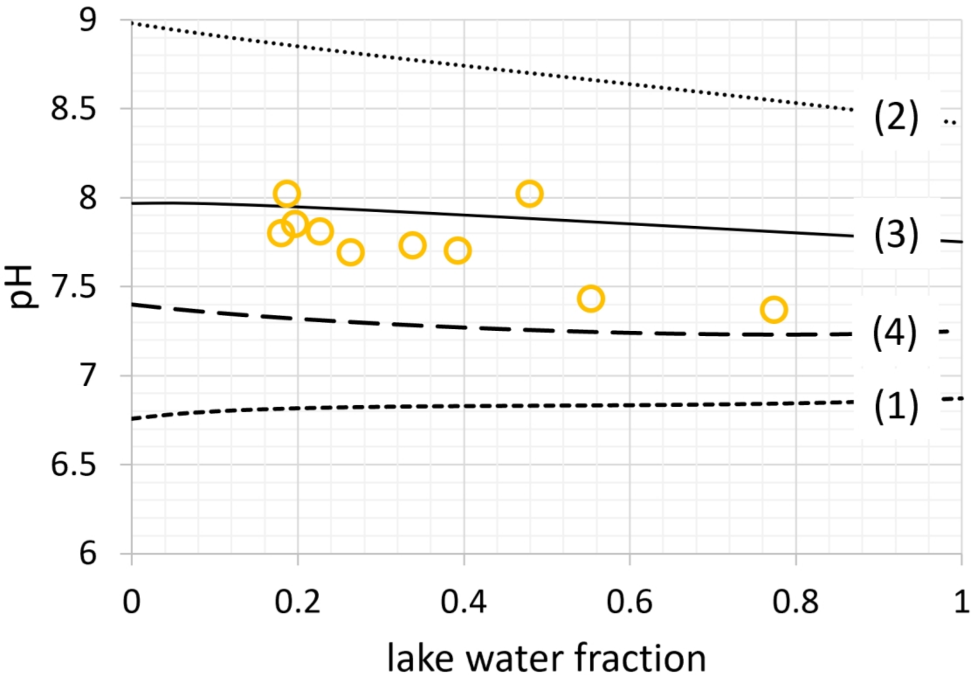

Figure 13. Yellow circles represent beach sample pH's plotted according to the lake water fraction. The lines depict pH trends according to end-member theoretical scenarios: (1) precipitation of aragonite with no CO2 degassing (kerolite remains undersaturated in the mixtures); (2) CO2 degassing to pCO2 of 3.5 without solid precipitation; (3) CO2 degassing to CO2 of 3.5 with solid precipitation; (4) no CO2 degassing and no mineral precipitation.

132x93mm (330 x 330 DPI)

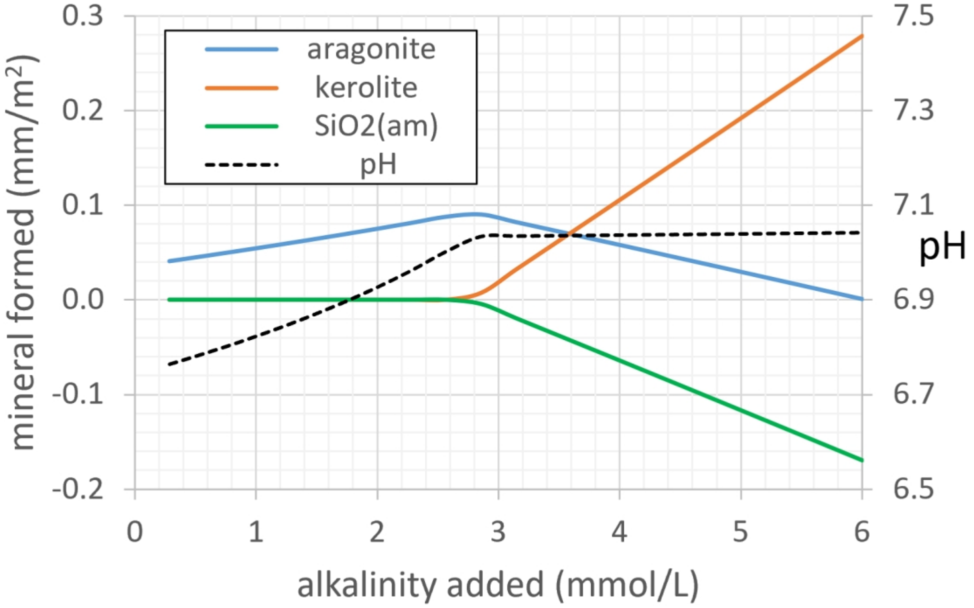

Figure 14. Thickness of solids formed (in mm of mineral/m2 surface/m of lake water depth) by the mixing of 50% of seepage water and 50% of lake water, and adding alkalinity from CO2 degassing, and microbial photosynthesis, and sulphate reduction. The simulation consider that silica is available from dissolution of dead diatom shells.

127x80mm (330 x 330 DPI)

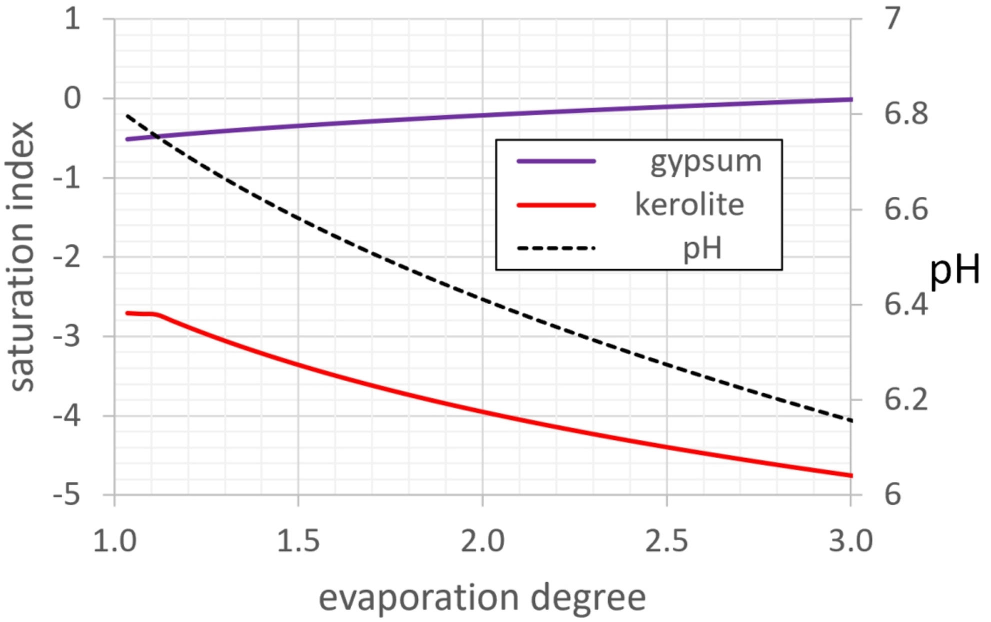

Figure 15. Evolution of saturation indices of gypsum and kerolite and pH values for a mixture of 80% of seepage and 20% of lake water that undergo concentration due to evaporation.

118x75mm (330 x 330 DPI)

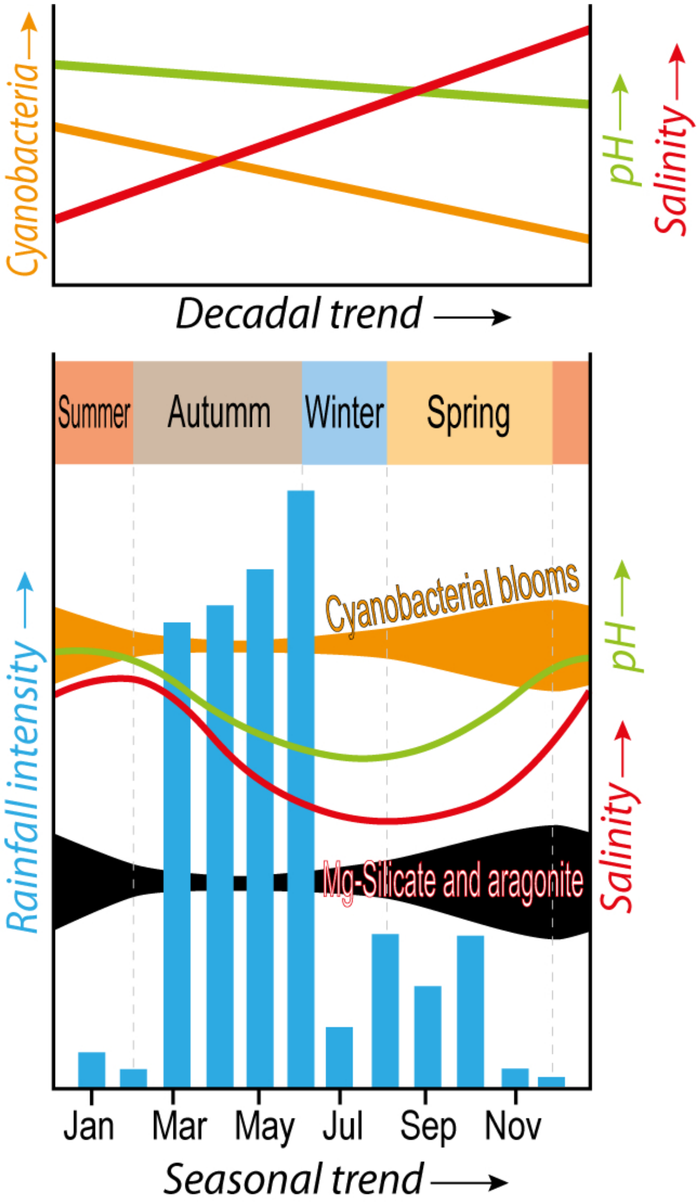

Figure 16. Sketches illustrating the decadal and seasonal trends in rainfall intensities, salinity gradients, pH fluctuations, cyanobacterial blooms, and putative Mg-silicate and aragonite precipitation patterns in Lake Clifton, Australia. The arrows indicate higher values. Based on data in Moore & Turner (1988); Rosen et al., (1996); Smith et al.,(2010); Forbes & Vogwill (2016), and herein.

54x93mm (300 x 300 DPI)

Supplementary Materials for:

Formation of Mg-silicates in the microbial sediments of a brackish, slightly alkaline coastal lake (Lake Clifton, Australia): environmental versus microbiological drivers

Ramon Mercedes-Martín*, Mónica Sánchez-Román, Carlos Ayora, Mike Rogerson, Camille Thomas, Alex Brasier, Rob Van Spanning, David Wacey, and John J. Reijmer

**Corresponding Author: ramon.mercedes@uab.cat*

This document contains 11 pages.

Figure S1. Aerial image from Google Earth satellite data (December 2016) showing the location of the water samples (black numbers) used in this work. For the detailed location of the water samples and soft substrates collected within the red square area, refer to Figure 1C.

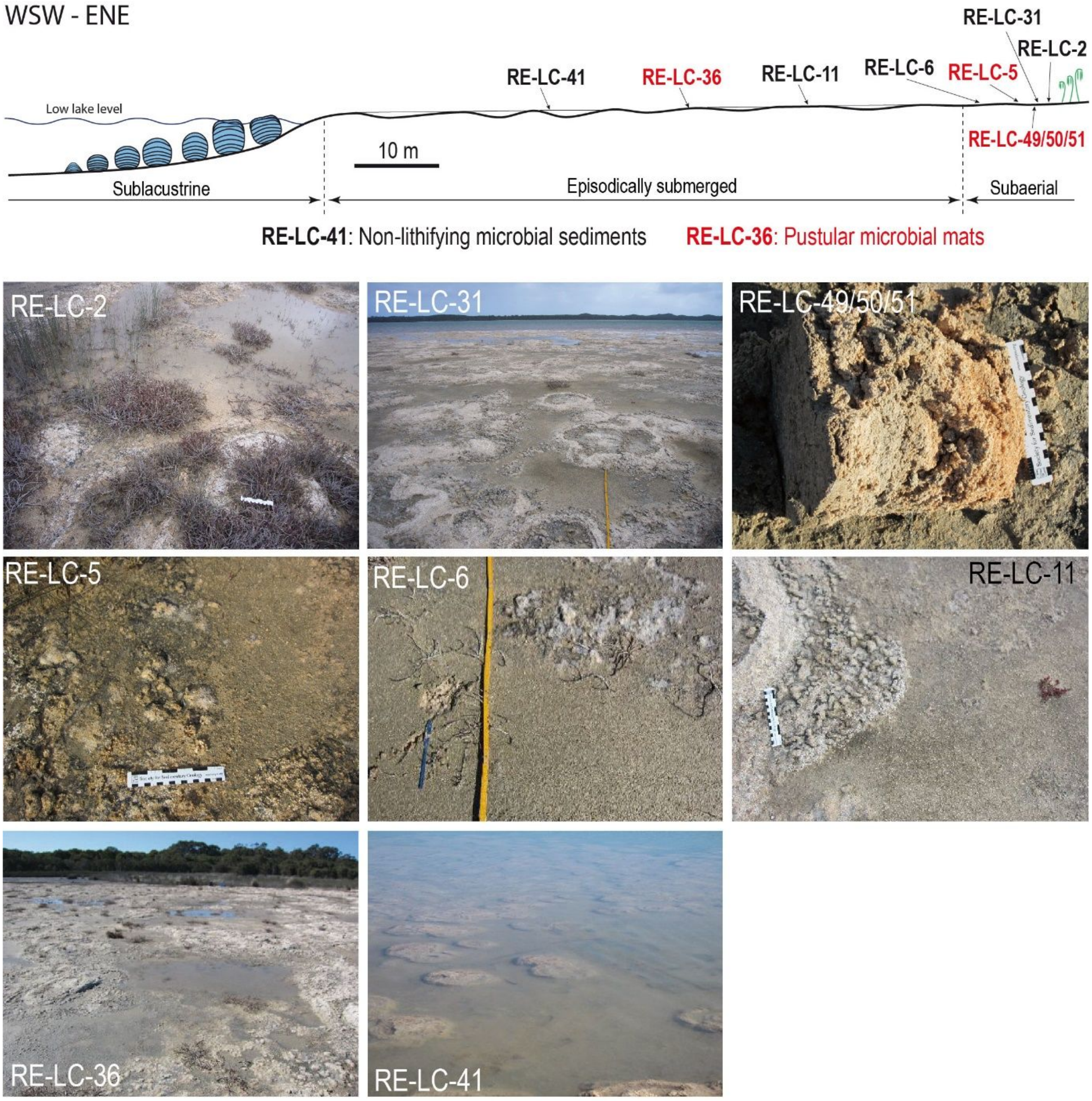

Figure S2. Depositional transect across lake Clifton sublacustrine to subaerial settings showing the location of the soft substrates studied (non-lithifying microbial sediments and pustular microbial mats). Pictures show the depositional features of the environments where the samples were collected.

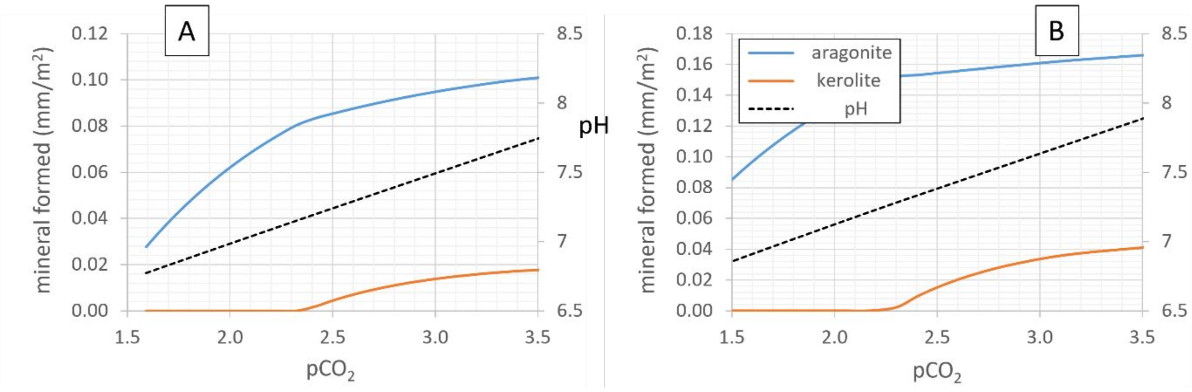

Figure S3. Thickness of solids formed (in mm of solid/m^2 surface/m of lake water depth), and CO_2 progressive degassing from: (A) a mixing of 20% seepage and 80% lake water, and (B) a mixing of 80% seepage and 20% lake water. Note that pCO_2 equals –log CO_2 pressure. Degasification progresses from left to right until it reaches atmospheric values (3.5).

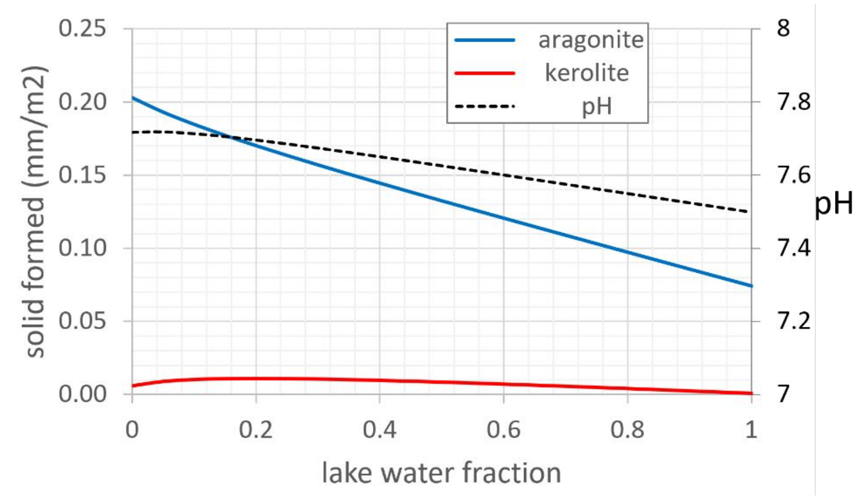

Figure S4. Thickness of solids formed (in mm of solid/m^2 surface/m of lake water depth) with respect to the mixing of seepage and lake water for a given pCO$_2$ of 3 (close to atmospheric pressure of 3.5).

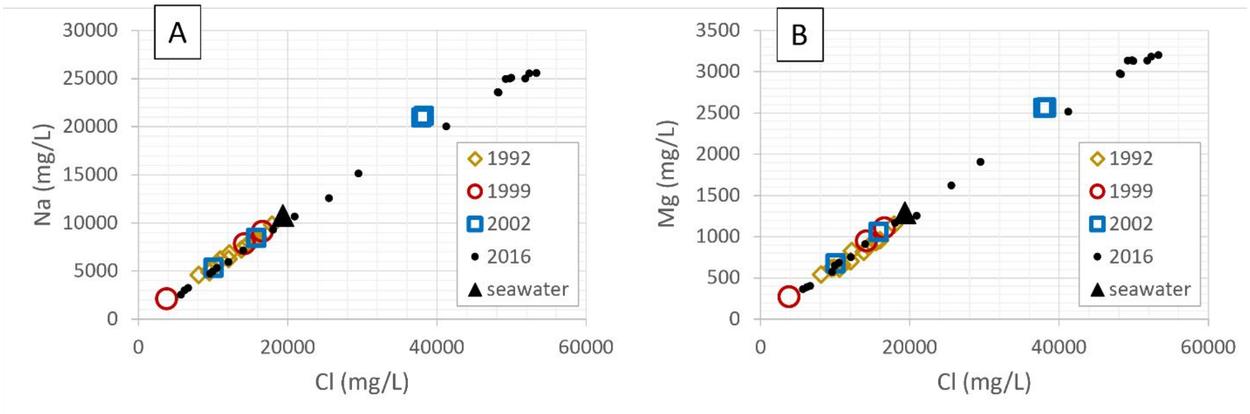

Figure S5. Correlation plots of the concentrations of Na (A) and Mg (B) with Cl in Lake Clifton waters showing binary mixing. The saline end member increases salinity along the decades. Data from Rosen et al. (1996) and Andreas Reimer in Caselmann (2005).

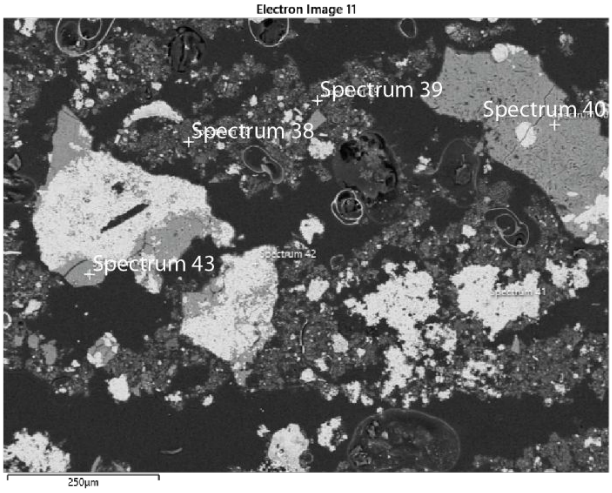

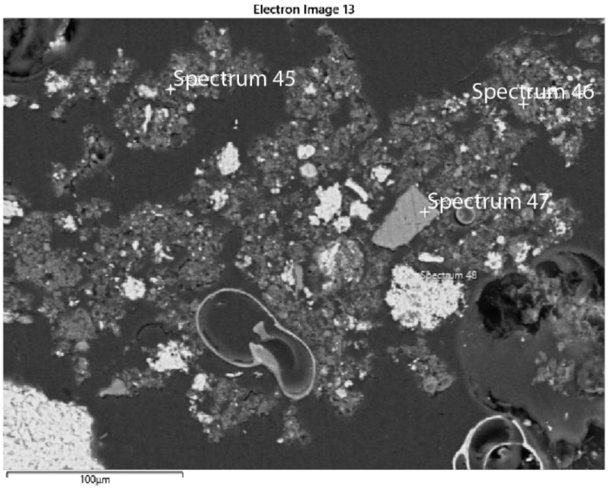

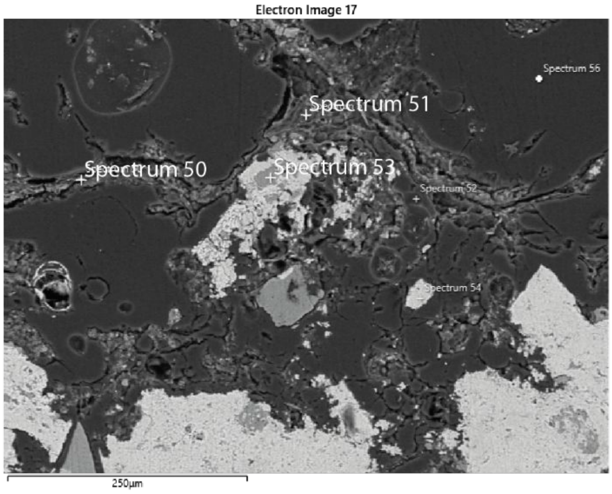

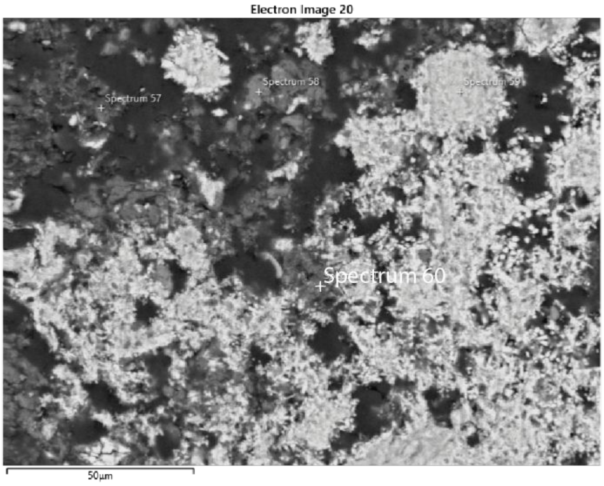

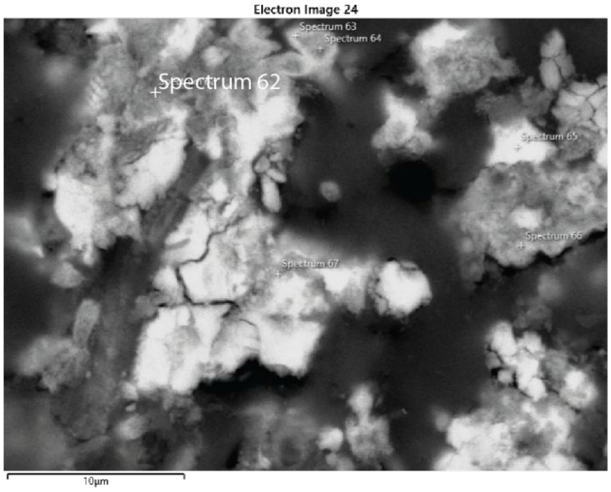

Spectrum number	Mg/Si ratio
38	0.68
39	0.60
40	0.69
43	0.69
45	0.60
46	0.61
47	0.66
50	0.66
51	0.58
53	0.76
60	0.80
62	0.69

Table S1. Mg/Si ratios on Mg-Si phases obtained from EDS measurements on diamond-polished thin section RE-LC-11, which corresponds to a non-lithifying microbial sediment collected from the episodically submerged environment.

Sample	Latitude	Longitude	Water type	Temp	pH	Alkalinity	Ca	K	Mg	SO4	Si	Na	Cl
9	32°43'45.46"S	115°39'4.03"E	seepage	14.6	7.21	409	324	72	386	575	21	2993	6217
24	32°43'56.96"S	115°39'2.24"E	seepage	15.9	8.02	351	282	71	400	671	25	3226	6666
25	32°43'52.83"S	115°39'0.54"E	seepage	13.8	7.4	668	721	61	363	157	35	2509	5728
1	32°44'0.34"S	115°39'3.72"E	beach	18.8	7.81	259	368	133	751	1284	11	5928	12102
2	32°43'42.78"S	115°38'55.95"E	beach	17.6	7.8	382	379	104	572	964	23	4734	9619
4	32°43'3.41"S	115°38'16.23"E	beach	12.7	7.7	678	745	264	1252	2042	19	10657	20957
5	32°43'57.66"S	115°39'1.13"E	beach	15.9	8.02	253	404	126	646	1120	18	4915	9966
15	32°44'43.37"S	115°39'16.80"E	beach	16.6	7.69	499	568	169	911	1597	11	7114	14056
16	32°43'57.84"S	115°38'59.89"E	beach	16.2	7.37	197	1062	463	2516	4457	7	20011	41272
17	32°43'56.96"S	115°39'2.24"E	beach	15.9	8.02	351	719	280	1620	2876	7	12568	25580
19	32°44'0.40"S	115°39'3.05"E	beach	17.1	7.85	389	337	129	681	1156	11	5294	10515
20	32°43'57.78"S	115°39'0.36"E	beach	16.4	7.43	235	833	350	1905	3399	9	15120	29516
26	32°44'0.51"S	115°39'2.16"E	beach	15.6	7.73	240	548	223	1167	2099	12	9297	18058
6	32°43'4.85"S	115°38'1.89"E	lake	15.9	7.25	129	1305	589	3136	5507	6	24963	49784
7	32°44'42.83"S	115°39'14.82"E	lake	15.3	7.25	259	1340	604	3201	5713	7	25578	53330
8	32°44'58.52"S	115°39'20.58"E	lake	15.3	7.02	111	1313	590	3132	5513	6	24930	49228
11	32°43'47.35"S	115°38'55.03"E	lake	13.6	6.87	128	1329	591	3126	5558	7	25086	49986
13	32°43'47.35"S	115°38'55.03"E	lake	13.4	7.07	151	1311	588	3134	5546	6	24981	51838
21	32°43'57.88"S	115°38'59.64"E	lake	15.9	7.29	234	1248	559	2969	5305	7	23525	48300
22	32°44'0.70"S	115°39'1.10"	lake	14.9	7.1	154	1240	547	2980	5271	7	23562	48147
23	32°43'4.85"S	115°38'1.89"E	lake	14.5	7.2	129	1330	592	3182	5696	6	25529	52395
			seawater		8.2	256	412	399	1292	2712	5	10768	19353

Table S2. Concentration (mg/L) of water samples collected from Lake Clifton between July and August 2016. Alkalinity in mg/L $CaCO_3$. Standard seawater according to Summerhayes and Thorpe (1996).

sample	Latitude	Longitude	Water type	Aragonite	Sepiolite(d)	Sepiolite	Stevensite	Kerolite	SiO2(am)	CO2(g)
9	32°43'45.46"S	115°39'4.03"E	seepage	0.11	-4.71	-2.09	-11.63	-3.42	-0.63	-1.81
24	32°43'56.96"S	115°39'2.24"E	seepage	0.78	-1.24	1.41	-6.43	1.78	-0.57	-2.70
25	32°43'52.83"S	115°39'0.54"E	seepage	0.88	-3.31	-0.72	-9.67	-1.46	-0.40	-1.78
1	32°44'0.34"S	115°39'3.72"E	beach	0.50	-2.64	0.10	-8.26	-0.05	-0.93	-2.64
2	32°43'42.78"S	115°38'55.95"E	beach	0.70	-1.94	0.76	-7.42	0.79	-0.61	-2.45
4	32°43'3.41"S	115°38'16.23"E	beach	0.97	-1.81	0.75	-7.32	0.89	-0.60	-2.18
5	32°43'57.66"S	115°39'1.13"E	beach	0.71	-1.29	1.36	-6.43	1.78	-0.70	-2.88
15	32°44'43.37"S	115°39'16.80"E	beach	0.80	-2.93	-0.26	-8.77	-0.56	-0.90	-2.25
16	32°43'57.84"S	115°38'59.89"E	beach	0.32	-3.44	-0.78	-9.45	-1.24	-0.98	-2.41
17	32°43'56.96"S	115°39'2.24"E	beach	0.99	-1.57	1.08	-6.65	1.56	-1.05	-2.82
19	32°44'0.40"S	115°39'3.05"E	beach	0.67	-2.56	0.12	-8.20	0.01	-0.92	-2.51
20	32°43'57.78"S	115°39'0.36"E	beach	0.33	-3.37	-0.70	-9.39	-1.18	-0.92	-2.37
26	32°44'0.51"S	115°39'2.16"E	beach	0.46	-2.41	0.23	-8.04	0.18	-0.84	-2.64
6	32°43'4.85"S	115°38'1.89"E	lake	0.13	-3.70	-1.05	-9.83	-1.62	-1.00	-2.48
7	32°44'42.83"S	115°39'14.82"E	lake	0.46	-3.40	-0.76	-9.42	-1.21	-0.91	-2.18
8	32°44'58.52"S	115°39'20.58"E	lake	-0.17	-4.63	-1.99	-11.23	-3.02	-0.99	-2.31
11	32°43'47.35"S	115°38'55.03"E	lake	-0.27	-5.00	-2.41	-11.87	-3.66	-0.90	-2.11
13	32°43'47.35"S	115°38'55.03"E	lake	0.01	-4.36	-1.78	-10.88	-2.67	-0.97	-2.24
21	32°43'57.88"S	115°38'59.64"E	lake	0.41	-3.44	-0.78	-9.46	-1.25	-0.94	-2.26
22	32°44'0.70"S	115°39'1.10"	lake	0.02	-4.19	-1.56	-10.61	-2.40	-0.93	-2.25
23	32°43'4.85"S	115°38'1.89"E	lake	0.09	-3.82	-1.21	-10.04	-1.83	-0.97	-2.44

Table S3. Saturation indices for some authigenic solid phases and log CO_2 pressure of the analyses reported in Table S2.

Sample	Latitude	Longitude	Temp	pH	Alkalinity	Ca	K	Mg	SO4	Si	Na	Cl	Ref
10.11.1987				8.96	130	274	231	760	1607		6831	12746	(A)
25.05.1991			18.0		175	432	329	1144	1851	16	9835	17897	(B)
03.10.1991			18.0	8.3	165	242	190	618	942	14	4900	9522	
08.11.1991			18.0		135	207	151	540	804	15	4584	8107	
06.12.1991			20.0	8.7	152	263	201	615	1026	17	5790	10570	
09.01.1992			21.0	8.7	155	286	223	702	1125	11	6244	12068	
07.02.1992			20.0	8.5	156	328	265	819	1335	16	7240	13805	
09.03.1192			19.5	8.4	138	347	262	879	1491	15	7650	14480	
07.04.1992			19.0	8.6	156	362	280	947	1557	15	8362	15704	
08.05.1992			18.5	8.2	154	378	282	957	1563	11	8547	16021	
09.06.1992			18.0	8.1	150	351	282	932	1629	13	8179	15447	
10.07.1992			17.0	7.9	156	308	264	829	1218	14	6839	12202	
12.08.1992			17.5	8.0	166	267	226	656	1089	14	6205	10941	
08.11.1992			18.0	8.1	160	244	194	623	864	14	5279	9804	
11.08.1998					175	441	266	1066	2240	13	8955	16173	(C)
11.08.1998			18.4	8.21	251	412	232	952	1984	13	7851	14204	
11.08.1998			20.9	8.42	422	196	59	275	560	27	2139	3789	
11.08.1998			16.7	8.22	204	448	271	1109	2321	13	9144	16590	
09.04.2002	32°44`540	115°39`08	18.5	8.34	110	442	118	670	1166	16	5298	10094	(C)
09.04.2002	32°44`541	115°39`08	19.9	8.08	163	563	206	1054	1787	22	8426	15840	
09.04.2002	32°44`542	115°39`079	20.1	7.96	160	1026	572	2555	5458	26	20925	37938	
09.04.2002	32°44`794	115°39	20.6	7.96	160	1025	651	2562	5439	26	21096	38301	

Table S4. Concentration (mg/L) of the water samples from Lake Clifton. Alkalinity in mg/L $CaCO_3$. Data from (A) Moore et al., 1987; (B) Rosen et al., 1996; (C) A. Reimer in Caselmann, 2005 (sampled in the beach/lake/ seepage near boardwalk).

Sample	Latitude	Longitude	Aragonite	Sepiolite(d)	Sepiolite	Stevensite	Kerolite	SiO2(am)	CO2(g)
12.07.1983									
10.11.1987			1.05	-4.40			-1.66		-4.23
25.05.1991									
03.10.1991			0.68	-0.57	2.14	-5.23	2.98	-0.84	-3.27
08.11.1991									
06.12.1991			1.00	1.17	3.94	-2.59	5.62	-0.80	-3.79
09.01.1992			1.04	0.72	3.51	-3.15	5.06	-0.99	-3.79
07.02.1992			0.91	0.60	3.37	-3.44	4.77	-0.80	-3.56
09.03.1192			0.78	0.20	2.95	-4.05	4.16	-0.81	-3.50
07.04.1992			0.99	1.03	3.77	-2.81	5.40	-0.82	-3.70
08.05.1992			0.68	-0.88	1.84	-5.64	2.57	-0.92	-3.23
09.06.1992			0.54	-1.08	1.63	-5.99	2.22	-0.84	-3.13
10.07.1992			0.33	-1.89	0.79	-7.25	0.96	-0.81	-2.89
12.08.1992			0.41	-1.71	0.99	-6.95	1.26	-0.82	-2.95
08.11.1992			0.48	-1.35	1.37	-6.40	1.81	-0.83	-3.06
11.08.1998									
11.08.1998			0.93	-0.67	2.06	-5.35	2.86	-0.85	-3.03
11.08.1998			1.28	0.11	2.90	-4.27	3.94	-0.61	-2.92
11.08.1998			0.84	-0.47	2.21	-5.10	3.11	-0.83	-3.15
09.04.2002	32°44`540	115°39`08	0.78	-0.19	2.54	-4.67	3.54	-0.78	-3.50
09.04.2002	32°44`541	115°39`08	0.78	-0.38	2.39	-4.99	3.22	-0.63	-3.07
09.04.2002	32°44`542	115°39`079	0.84	0.50	3.27	-3.71	4.50	-0.45	-3.05
09.04.2002	32°44`794	115°39	0.85	0.51	0.51	-3.69	4.52	-0.46	-3.05

Table S5. Saturation indices for some authigenic solid phases and log CO_2 pressure of the analyses reported in Table S4.